


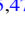





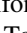
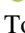
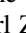
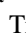





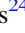
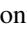

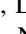






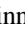
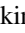

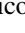

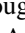

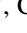
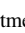
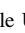
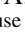


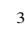
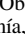
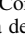
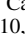





TOI 564 b and TOI 905 b: Grazing and Fully Transiting Hot Jupiters Discovered by TESS

Allen B. Davis^{1,45} , Songhu Wang^{1,46} , Matias Jones^{2,3}, Jason D. Eastman⁴ , Maximilian N. Günther^{5,47} , Keivan G. Stassun^{6,7} , Brett C. Addison⁸ , Karen A. Collins⁴ , Samuel N. Quinn⁴ , David W. Latham⁴ , Trifon Trifonov⁹ , Sahar Shahaf¹⁰, Tsevi Mazeh¹¹ , Stephen R. Kane¹² , Norio Narita^{13,14,15,16} , Xian-Yu Wang^{17,18} , Thiam-Guan Tan¹⁹ , David R. Ciardi²⁰ , Andrei Tokovinin²¹ , Carl Ziegler²² , René Tronsgaard²³ , Sarah Millholland^{1,45} , Bryndis Cruz¹, Perry Berlind⁴, Michael L. Calkins⁴ , Gilbert A. Esquerdo⁴ , Kevin I. Collins²⁴ , Dennis M. Conti²⁵ , Felipe Murgas^{26,27}, Phil Evans²⁸ , Pablo Lewin²⁹ , Don J. Radford³⁰, Leonardo A. Paredes³¹, Todd J. Henry³² , James Hodari-Sadiki³¹, Michael B. Lund²⁰ , Jessie L. Christiansen²⁰ , Nicholas M. Law³³ , Andrew W. Mann³³ , César Briceño²¹, Hannu Parviainen^{34,35} , Enric Palle^{34,35} , Noriharu Watanabe^{13,15,36} , George R. Ricker⁵ , Roland Vanderspek⁵ , Sara Seager^{5,37,38} , Joshua N. Winn³⁹ , Jon M. Jenkins⁴⁰ , Akshata Krishnamurthy⁵ , Natalie M. Batalha⁴¹ , Jennifer Burt⁴² , Knicole D. Colón⁴³ , Scott Dynes⁵ , Douglas A. Caldwell⁴⁴ , Robert Morris⁴⁴, Christopher E. Henze⁴⁰, and Debra A. Fischer¹ 

¹ Department of Astronomy, Yale University, 52 Hillhouse Avenue, New Haven, CT 06511, USA; allen.b.davis@yale.edu

² European Southern Observatory, Alonso de Córdova 3107, Vitacura, Casilla 19001, Santiago, Chile

³ Instituto de Astronomía, Universidad Católica del Norte, Angamos 0610, 1270709, Antofagasta, Chile

⁴ Center for Astrophysics | Harvard & Smithsonian, 60 Garden Street, Cambridge, MA 02138, USA

⁵ Department of Physics and Kavli Institute for Astrophysics and Space Research, Massachusetts Institute of Technology, Cambridge, MA 02139, USA

⁶ Department of Physics and Astronomy, Vanderbilt University, Nashville, TN 37235, USA

⁷ Department of Physics, Fisk University, Nashville, TN 37208, USA

⁸ University of Southern Queensland, Centre for Astrophysics, West Street, Toowoomba, QLD 4350 Australia

⁹ Max-Planck-Institut für Astronomie, Königstuhl 17, D-69117 Heidelberg, Germany

¹⁰ School of Physics and Astronomy, Tel-Aviv University, Tel Aviv 69978, Israel

¹¹ School of Physics and Astronomy, Raymond and Beverly Sackler Faculty of Exact Sciences, Tel Aviv University, Tel Aviv 6997801, Israel

¹² Department of Earth and Planetary Sciences, University of California, Riverside, CA 92521, USA

¹³ Astrobiology Center, 2-21-1 Osawa, Mitaka, Tokyo 181-8588, Japan

¹⁴ JST, PRESTO, 2-21-1 Osawa, Mitaka, Tokyo 181-8588, Japan

¹⁵ National Astronomical Observatory of Japan, 2-21-1 Osawa, Mitaka, Tokyo 181-8588, Japan

¹⁶ Instituto de Astrofísica de Canarias (IAC), E-38205 La Laguna, Tenerife, Spain

¹⁷ National Astronomical Observatories, Chinese Academy of Sciences, Beijing 100012, People's Republic of China

¹⁸ University of Chinese Academy of Sciences, Beijing, 100049, People's Republic of China

¹⁹ Perth Exoplanet Survey Telescope, Perth, WA, Australia

²⁰ NASA Exoplanet Science Institute-Caltech/IPAC, 1200 East California Boulevard, Pasadena, CA 91125, USA

²¹ Cerro Tololo Inter-American Observatory, Casilla 603, La Serena, Chile

²² Dunlap Institute for Astronomy and Astrophysics, University of Toronto, 50 St. George Street, Toronto, ON M5S 3H4, Canada

²³ DTU Space, National Space Institute, Technical University of Denmark, Elektrovej 328, DK-2800 Kgs. Lyngby, Denmark

²⁴ George Mason University, 4400 University Drive, Fairfax, VA 22030, USA

²⁵ American Association of Variable Star Observers, 49 Bay State Road, Cambridge, MA 02138, USA

²⁶ Instituto de Astrofísica de Canarias (IAC), E-38205 La Laguna, Tenerife, Spain

²⁷ Departamento de Astrofísica, Universidad de La Laguna (ULL), E-38206 La Laguna, Tenerife, Spain

²⁸ El Sauce Observatory, Chile

²⁹ The Maury Lewin Astronomical Observatory, Glendora, CA 91741, USA

³⁰ Brierfield Observatory, New South Wales, Australia

³¹ Physics and Astronomy Department, Georgia State University, Atlanta, GA 30302, USA

³² RECONS Institute, Chambersburg, PA, USA

³³ Department of Physics and Astronomy, The University of North Carolina at Chapel Hill, Chapel Hill, NC 27599, USA

³⁴ Instituto de Astrofísica de Canarias (IAC), E-38200 La Laguna, Tenerife, Spain

³⁵ Dept. Astrofísica, Universidad de La Laguna (ULL), E-38206 La Laguna, Tenerife, Spain

³⁶ Department of Astronomical Science, The Graduate University for Advanced Studies, SOKENDAI, 2-21-1 Osawa, Mitaka, Tokyo 181-8588, Japan

³⁷ Department of Earth, Atmospheric, and Planetary Sciences, Massachusetts Institute of Technology, Cambridge, MA 02139, USA

³⁸ Department of Aeronautics and Astronautics, Massachusetts Institute of Technology, Cambridge, MA 02139, USA

³⁹ Department of Astrophysical Sciences, Princeton University, 4 Ivy Lane, Princeton, NJ 08544, USA

⁴⁰ NASA Ames Research Center, Moffett Field, CA 94035, USA

⁴¹ University of California, Santa Cruz, CA, USA

⁴² Jet Propulsion Laboratory, California Institute of Technology, 4800 Oak Grove Drive, Pasadena, CA 91109, USA

⁴³ Exoplanets and Stellar Astrophysics Laboratory, Code 667, NASA Goddard Space Flight Center, Greenbelt, MD 20771, USA

⁴⁴ SETI Institute/NASA Ames Research Center, USA

Received 2019 December 20; revised 2020 June 26; accepted 2020 June 29; published 2020 October 29

Abstract

We report the discovery and confirmation of two new hot Jupiters discovered by the Transiting Exoplanet Survey Satellite (TESS): TOI 564 b and TOI 905 b. The transits of these two planets were initially observed by TESS with

⁴⁵ National Science Foundation Graduate Research Fellow.

⁴⁶ 51 Pegasi b Fellow.

⁴⁷ Juan Carlos Torres Fellow.

orbital periods of 1.651 and 3.739 days, respectively. We conducted follow-up observations of each system from the ground, including photometry in multiple filters, speckle interferometry, and radial velocity measurements. For TOI 564 b, our global fitting revealed a classical hot Jupiter with a mass of $1.463_{-0.096}^{+0.10} M_J$ and a radius of $1.02_{-0.29}^{+0.71} R_J$. Also a classical hot Jupiter, TOI 905 b has a mass of $0.667_{-0.041}^{+0.042} M_J$ and radius of $1.171_{-0.051}^{+0.053} R_J$. Both planets orbit Sun-like, moderately bright, mid-G dwarf stars with $V \sim 11$. While TOI 905 b fully transits its star, we found that TOI 564 b has a very high transit impact parameter of $0.994_{-0.049}^{+0.083}$, making it one of only ~ 20 known systems to exhibit a grazing transit and one of the brightest host stars among them. Therefore, TOI 564 b is one of the most attractive systems to search for additional nontransiting, smaller planets by exploiting the sensitivity of grazing transits to small changes in inclination and transit duration over a timescale of several years.

Unified Astronomy Thesaurus concepts: [Exoplanet astronomy \(486\)](#); [Exoplanet detection methods \(489\)](#); [Radial velocity \(1332\)](#); [Transit photometry \(1709\)](#); [Extrasolar gas giants \(509\)](#); [Hot Jupiters \(753\)](#)

Supporting material: data behind figures

1. Introduction

Transiting hot Jupiters are among the best-studied and most mysterious classes of exoplanets. Despite the discovery, confirmation, and characterization of hundreds of these worlds, questions persist as to their mechanisms of formation and orbital evolution. It is not known, for instance, whether hot Jupiters formed beyond the ice line and migrated inward (Lin et al. 1996), or whether they formed close to their present-day orbits (Bodenheimer et al. 2000; Batygin et al. 2016). Are they connected evolutionarily to warm Jupiters (Huang et al. 2016)? What can we infer about the presence of planetary companions to hot Jupiters, which evidence suggests are rare close to the star (Becker et al. 2015; Millholland et al. 2016; Cañas et al. 2019b) but relatively common farther out (Knutson et al. 2014)? What can the atmospheres of hot Jupiters, which are best studied through transit and eclipse observations, tell us about their formation scenarios (e.g., Öberg et al. 2011; Sing et al. 2016)?

Our empirical knowledge of hot Jupiters is based on the foundation of our small but growing sample of these worlds (currently numbering ~ 250). While small, rocky planets are understood to be present, on average, around every star (e.g., Fressin et al. 2013; Petigura et al. 2018), various studies have found that on the order of only $\sim 0.5\%$ of stars host a hot Jupiter (e.g., Howard et al. 2012; Petigura et al. 2018; Zhou et al. 2019), $\sim 10\%$ of which will have a geometry resulting in a visible transit. Transiting hot Jupiters are therefore intrinsically rare; so, given the broad and abiding questions surrounding them, there is value in each additional example found, particularly around stars that are amenable to follow-up observations.

The Rossiter–McLaughlin (RM) effect (Holt 1893; Schlesinger 1910; McLaughlin 1924; Rossiter 1924) allows measurement of the sky-projected angle λ between a planet’s orbital plane and its host star’s equator (e.g., Queloz et al. 2000; Addison et al. 2018). The RM measurements are most sensitive in systems with deep transits of a planet orbiting a bright or rapidly rotating star. By measuring spin–orbit alignments of many systems, we can probe the processes involved in the formation and migration of exoplanets (e.g., Lin et al. 1996; Bodenheimer et al. 2000; Ford & Rasio 2008; Naoz et al. 2011; Wu & Lithwick 2011), in particular hot (Crida & Batygin 2014; Winn & Fabrycky 2015) and warm (Dong et al. 2014) Jupiters and compact transiting multiplanet systems (Albrecht et al. 2013; Wang et al. 2018).

While the Kepler (Borucki et al. 2010) and K2 (Howell et al. 2014) missions together examined only $\sim 5\%$ of the sky, the Transiting Exoplanet Survey Satellite (TESS) mission (Ricker et al. 2015) is conducting a survey of $\sim 80\%$ of the sky,

scanning sector by sector for transit signals around the brightest and nearest stars. After TESS completes its survey, we will have identified nearly all of the most observationally favorable transiting hot Jupiters that will ever be available to astronomers. Therefore, these planets will serve as the best possible sample for testing the myriad open questions surrounding hot Jupiters.

To date, five new hot Jupiters initially detected by TESS have been confirmed: HD 202772A b (Wang et al. 2019), HD 2685 b (Jones et al. 2019), TOI 150 b (Cañas et al. 2019a; Kossakowski et al. 2019), HD 271181 b (Kossakowski et al. 2019), and TOI 172 b (Rodriguez et al. 2019). Additionally, the HATNet survey (Bakos et al. 2004) detected two transiting hot Jupiter candidates in 2010, HATS-P-69 b and HATS-P-70 b, which were later observed by TESS, leading to their confirmation (Zhou et al. 2019).

A grazing transit is a transit in which only part of the planet’s projected disk occults the stellar disk (formally stated with the grazing transit condition, $b + R_p/R_{\text{star}} > 1$, where b is the impact parameter, and R_p and R_{star} are the radii of the planet and star, respectively). Such systems are observationally rare; of the more than 3000 known transiting planets, only about half a percent exhibit a grazing transit at the 1σ level or higher (NASA Exoplanet Archive;⁴⁸ Akeson et al. 2013). TESS has detected one grazing transiting planet so far: TOI 216 b, a warm giant planet with an outer companion near the 2:1 resonance, orbiting a $V = 12.4$ star (Dawson et al. 2019).

Grazing transiting systems present both upsides and downsides for a system’s characterization prospects. On the one hand, the planetary radius is more difficult to measure because of the covariance between the planet size and other transit parameters (primarily the impact parameter) compared to a fully transiting system. For this reason, the inferred radius should perhaps be viewed only as a lower limit with high confidence. Furthermore, grazing systems will exhibit lower RM amplitudes because they cover less of the rotating star’s surface compared to a fully transiting planet.

On the other hand, grazing transits afford unique opportunities to probe other aspects of the system. Ribas et al. (2008) attempted to exploit the near-grazing transits of the hot Neptune GJ 436 b (Butler et al. 2004) to infer perturbations in the orbital inclination caused by interactions with a putative nontransiting outer planet, GJ 436 c, in a 2:1 mean-motion resonance. It was later found that the proposed planet was on an unstable orbit (Bean & Seifahrt 2008; Demory et al. 2009), and there was a lack of expected transit timing variation signals

⁴⁸ <http://exoplanetarchive.ipac.caltech.edu>

in future transits (Alonso et al. 2008; Pont et al. 2009; Winn 2009). Nevertheless, the underlying methodology is sound. A close-in hot Jupiter, for instance, will experience a precession in both its periastron and its line of nodes when an additional planet is present in the system. These precessions cause impact parameter variations, which, in the case of grazing transits, change both the transit duration and transit depth dramatically. Systems with grazing transits are therefore prime candidates when seeking to detect nontransiting exoplanets (e.g., Miralda-Escudé 2002) and even exomoons (Kipping 2009, 2010).

WASP-34 b (Smalley et al. 2011), a hot sub-Saturn, was the first planet discovered to have a likely grazing transit (with a confidence of 80%), and its host star remains the brightest known grazing transit host at $V = 10.3$. Other notable grazing transiting planets include hot Jupiters such as HAT-P-27 b/WASP-40 b (Béky et al. 2011/Anderson et al. 2011), WASP-45 b (Anderson et al. 2012), Kepler-434 b (Almenara et al. 2015), Kepler-447 b (Lillo-Box et al. 2015), K2-31 b (Grziwa et al. 2016), WASP-140 b (Hellier et al. 2017), Qatar-6b (Alsubai et al. 2018), NGTS-1 b (Bayliss et al. 2018), and WASP-174 b (Temple et al. 2018; Mancini et al. 2020). A pair of sub-Saturns, WASP-67 b (Hellier et al. 2012; Bruno et al. 2018) and CoRoT-25 b (Almenara et al. 2013), are the smallest known grazing transiting planets.

In this work, we report the discovery and confirmation of two new hot Jupiters detected by TESS, each around relatively bright ($V \sim 11$) stars: TOI 564 b and TOI 905 b. Particularly noteworthy is that TOI 564 is one of the brightest hosts of a grazing transiting planet, making it highly amenable to follow-up observations. Section 2 describes the observations and data reduction methods. Section 3 details the stellar parameters for the host stars. Section 4 presents planetary and system parameters from global analyses. Section 5 summarizes these results and places them in context.

2. Observation and Data Reduction

2.1. TESS Photometry

From 2019 February 2 to 2019 February 27, TOI 564 (TIC 1003831, TYC 6012-1100-1) was observed by TESS in sector 8 by CCD 4 on camera 2. From 2019 May 21 to 2019 June 18, TOI 905 (TIC 261867566, TYC 9266-362-1) was observed by TESS in sector 12 by CCD 1 on camera 2. Neither target will be observed again as part of TESS's primary mission. The basic parameters for both targets are given in Table 1.

The photometric data were analyzed with the Science Processing Operations Center (SPOC) pipeline (Jenkins et al. 2016) by NASA Ames Research Center. The data have a cadence of 2 minutes, and there is a gap of 6 days in the case of TOI 564 and 1 day in the case of TOI 905. TESS's CCD pixels have an on-sky size of $21''$. The SPOC pipeline produces two types of light curves: the simple aperture photometry (SAP) light curves, which are corrected for background effects, and the presearch data conditioning (PDCSAP) light curves (Smith et al. 2012; Stumpe et al. 2014), which are additionally corrected for systematics that appear in reference stars.

An automated data validation report (described in Twicken et al. 2018) was created for the PDCSAP light curve of both of our targets, revealing 11 transits on TOI 564 with a period of 1.65114 days and six transits with a period of 3.7395 days for

Table 1
Basic Observational Parameters

Parameter	TOI 564	TOI 905	Source
R.A. (hh:mm:ss)	08:41:10.8368	15:10:38.0821	Gaia DR2
Decl. (dd:mm:ss)	-16:02:10.7789	-71:21:41.8739	Gaia DR2
μ_α (mas yr ⁻¹)	-2.508 ± 0.050	-25.839 ± 0.033	Gaia DR2
μ_δ (mas yr ⁻¹)	-11.025 ± 0.04 2	-41.150 ± 0.051	Gaia DR2
Parallax (mas)	4.982 ± 0.031	6.274 ± 0.028	Gaia DR2
TESS (mag)	10.670 ± 0.006	10.572 ± 0.006	TIC V8
B (mag)	11.946 ± 0.138	12.358 ± 0.151	Tycho
V (mag)	11.175 ± 0.103	11.192 ± 0.071	Tycho
J (mag)	10.044 ± 0.030	9.890 ± 0.020	2MASS
H (mag)	9.710 ± 0.030	9.510 ± 0.020	2MASS
K (mag)	9.604 ± 0.020	9.448 ± 0.020	2MASS
$W1$ (mag)	9.562 ± 0.023	9.372 ± 0.022	AllWISE
$W2$ (mag)	9.598 ± 0.020	9.433 ± 0.019	AllWISE
$W3$ (mag)	9.587 ± 0.041	9.291 ± 0.030	AllWISE
$W4$ (mag)	...	9.151 ± 0.533	AllWISE
G (mag)	11.142 ^a	11.081 ^a	Gaia DR2
G_{BP} (mag)	11.527 ^a	11.509 ^a	Gaia DR2
G_{RP} (mag)	10.622 ^a	10.528 ^a	Gaia DR2

Note.

^a For global fitting, we adopted an uncertainty of 0.020 for each Gaia magnitude.

TOI 905. This preliminary analysis gave a companion radius of $1.22 \pm 0.16 R_J$ for TOI 905, consistent with a hot Jupiter. For TOI 564, the pipeline gave a companion radius of $0.49 \pm 0.24 R_J$, but the impact parameter was extremely poorly constrained; we would later find that this impact parameter was near unity, consistent with a grazing transit, so our ultimate measurement of the planetary radius was substantially larger than the initial estimate (see Section 4). Overall, both reports gave highly dispositive results in favor of the planetary hypothesis. The tests used included (for TOI 564 and TOI 905, respectively) the odd–even test (2.1σ and 1.6σ difference), the weak secondary test (3σ and 2σ for the maximum secondary peak), the statistical bootstrap test (extrapolated FAP $\sim 3 \times 10^{-96}$ and $<10^{-97}$), the ghost diagnostic test (core-to-halo ratio of 3.6 and 5.9), and, perhaps most importantly, the difference image centroid offsets from either the TIC position or the out-of-transit centroid ($2''$ in both cases, which is one-tenth of a pixel). The difference images are also extremely clean and consistent with the difference image centroids, demonstrating that each transit source is collocated with the target star image to within the resolution of the survey image.

To remove any stellar variability and other systematics that remained in the PDCSAP light curves, we further detrended the data using the following approach (see, e.g., Günther et al. 2017, 2018). First, we masked out the in-transit data. Then, we trained a Gaussian process (GP) model with a Matern 3/2 kernel and a white-noise kernel on the out-of-transit data using the CELERITE package (Foreman-Mackey et al. 2017a). After constraining the hyperparameters of the GP this way, we applied the GP to detrend the entire light curve. The resulting phase-folded TESS light curves near the transits of TOI 564 and TOI 905 are shown in orange in Figures 1 and 2, respectively. For TOI 564, the final Markov Chain Monte Carlo (MCMC) results for the GP Matern 3/2 fit to the light curve were $\log \sigma = -7.51^{+0.21}_{-0.15}$, $\log \rho = -0.49^{+0.35}_{-0.30}$, and $\log (y_{\text{err}}) = -6.5780^{+0.0068}_{-0.0070}$. For TOI 905, the results for

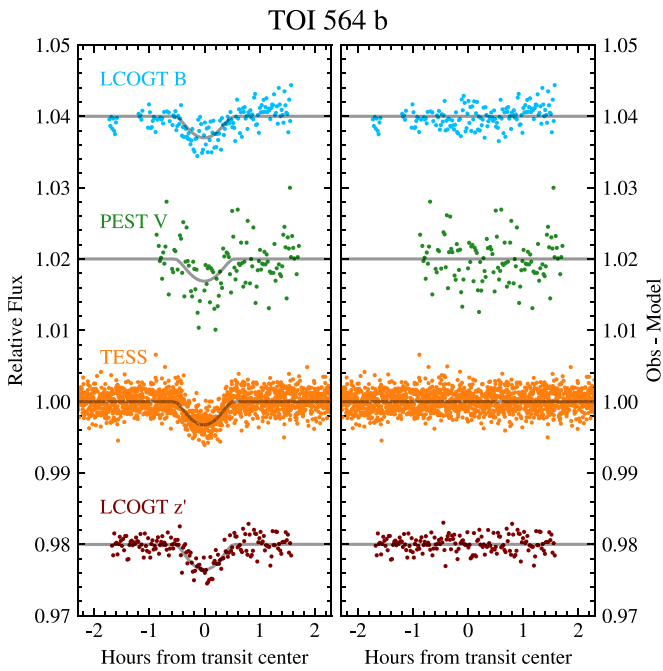


Figure 1. Left: transits of TOI 564 b. Blue shows an LCO-SSO B -band light curve from 2019 May 15 (Section 2.2.1). Green shows a PEST V -band light curve from 2019 May 10 (Section 2.2.3). Orange shows the detrended and phase-folded light curve of 11 transits from TESS (Section 2.1). Maroon shows an LCO-CTIO z' -band light curve from 2019 April 13 (Section 2.2.1). The model corresponding to each light curve’s filter is shown in gray (Section 4). Right: residuals obtained by subtracting the model from the observed transits. (The data used to create this figure are available.)

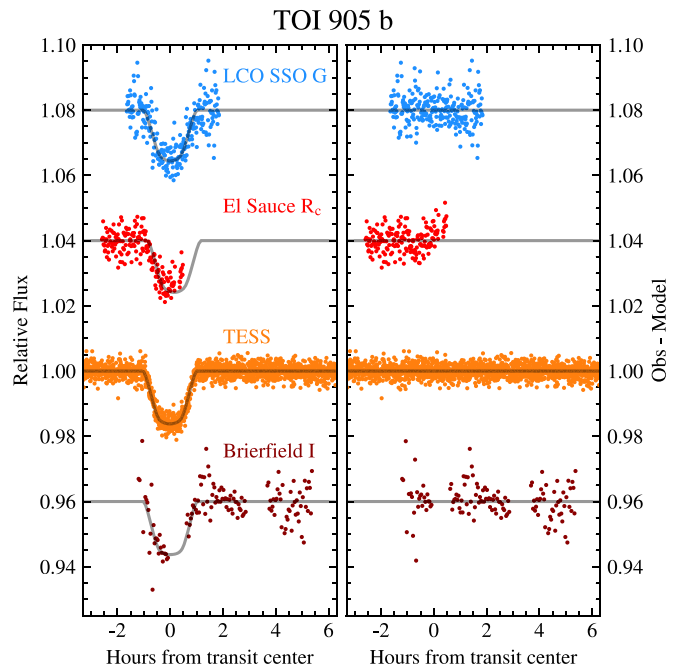


Figure 2. Left: transits of TOI 905 b. Blue shows an LCO-SSO G -band light curve from 2019 July 27 (Section 2.2.1). Red shows an El Sauce R_c -band light curve from 2019 July 31 (Section 2.2.5). Orange shows the detrended and phase-folded light curve of 11 transits from TESS (Section 2.1). Maroon shows a Brierfield I -band light curve from 2019 July 27 (Section 2.2.4). The model corresponding to each light curve’s filter is shown in gray (Section 4). Right: residuals obtained by subtracting the model from the observed transits. (The data used to create this figure are available.)

the GP were $\log \sigma = -8.02^{+0.15}_{-0.13}$, $\log \rho = -0.31 \pm 0.26$, and $\log (\gamma_{\text{err}}) = -6.2947^{+0.0052}_{-0.0053}$.

2.2. Ground-based Transit Photometry

Ground-based photometric follow-up observations were used both to confirm that the transit signals detected by TESS were indeed on the correct stars (TIC 1003831 and TIC 261867566) and to ensure that the detections were robust in multiple bands. Four distinct transits of TOI 564 were observed between 2019 April 13 and 2019 May 15 in three unique bands from four ground-based telescopes. Two distinct transits of TOI 905 were observed on July 27 and 31 in three unique bands from three ground-based telescopes. Figures 1 and 2 show the light curves for each transit observed for TOI 564 and TOI 905, respectively.

We used TESS Transit Finder, which is a customized version of the Tapir software package (Jensen 2013), to schedule all of the following photometric time-series follow-up observations. Table 2 gives a summary of the observations, which are described in detail in the following sections.

2.2.1. Las Cumbres Observatory Global Telescope

We acquired ground-based time-series follow-up photometry of full transits of TOI 564 on 2019 April 13 in the z' band and 2019 May 15 in the B band from two Las Cumbres Observatory Global Telescope (LCOGT) 1.0 m telescopes (Brown et al. 2013) located at Cerro Tololo Inter-American Observatory (CTIO) and Siding Spring Observatory (SSO), respectively. Additionally, we observed a full transit of

TOI 905 on 2019 July 27 using the LCOGT 0.4 m telescope at SSO in the G band. All images were calibrated by the standard LCOGT BANZAI pipeline, and the photometric data were extracted using the AstroImageJ (AIJ) software package (Collins et al. 2017). The two 1.0 m telescopes used for TOI 564 are each equipped with a 4096×4096 pixel LCO SINISTRO camera, which each have an image scale of $0''.389 \text{ pixel}^{-1}$. The 0.4 m telescope at SSO used an SBIG 6303 camera with an image scale of $0''.571 \text{ pixel}^{-1}$. For TOI 564, 165 images were acquired during the 195 minute observation in the z' band, and 169 images were acquired over the 199 minute observation in the B band. For the G -band transit of TOI 905, 278 images were taken over 228 minutes.

The TOI 564 light curves show clear transit detections using apertures with radii of $\sim 5''.5$. The nearest known Gaia DR2 (Gaia Collaboration et al. 2018) star is $23''$ from TOI 564 and 7.2 mag fainter. The FWHMs of the target and nearby stars are $\sim 1''.7$ and $\sim 2''.0$ in the z and B bands, respectively, so the follow-up aperture is negligibly contaminated by known nearby Gaia DR2 stars. The z' - and B -band light curves show events having depths consistent with the TESS depth within the uncertainties.

The TOI 905 light curve also shows a clear transit detection that is consistent with the TESS light curve using a photometric aperture with a radius of $8''.5$. Gaia DR2 finds that there is a star that is 6.1 mag fainter located $2''.2$ away from TIC 261867566.

2.2.2. Maury Lewin Astronomical Observatory

We observed a transit of TOI 564 b on 2019 May 2 from the Maury Lewin Astronomical Observatory (MLAO), a home

Table 2
Ground-based Transit Photometric Observations

Telescope	Camera	Filter	Pixel Scale (arcsec)	Est. PSF (arcsec)	Aperture Radius (pixel)	Date (UT)	Duration (minutes)	No. of Obs.	σ (ppt)
TOI 564									
LCO-CTIO (1 m)	Sinistro	z'	0.389	1.68	15	2019 Apr 13	195	165	0.9
MLAO (0.356 m)	STF-8300M	B	0.839	4.26	9	2019 May 2	82.2	48	12.0
PEST (0.3 m)	ST-8XME	V	1.23	4.1	7	2019 May 10	155	122	3.0
LCO-SSO (1 m)	Sinistro	B	0.389	2.04	14	2019 May 15	199	169	1.0
TCS (1.52 m)	MuSCAT2	g', r', i', z'	0.44	2.7, 3.5	8, 10	2020 Jan 13	60	200	3.8–4.8
TOI 905									
LCO-SSO (0.4 m)	SBIG 6303	g	0.571	9.59	15	2019 Jul 27	228	278	2.5
Brierfield (0.36 m)	Moravian 16803	I	1.47	4.7	6	2019 Jul 27	452	137	1.7
El Sauce (0.36 m)	STT1603-3	R_c	1.47	4.46	6	2019 Jul 31	184	186	1.4

observatory located in Glendora, California, USA, using a 0.356 m F10 Schmidt–Cassegrain Celestron C-14 Edge HD telescope with an SBIG STF-8300 detector and a B -band filter. The transit was observed at relatively high airmass, ranging from ~ 2 to ~ 3 , which resulted in low precision (~ 12.0 ppt) and a large trend in the time-series data. We fitted and removed this airmass trend and found that the transit’s depth and shape were generally consistent with the other three ground-based transits within the large error bars. Because of the lower precision of this transit observation compared to the other B -band transit observed by LCO-SSO, we ultimately do not include the MLAO data in the global fitting in Section 4.

2.2.3. Perth Exoplanet Survey Telescope

We observed a full transit of TOI 564 b on 2019 May 10 in the V band from the 0.3 m Perth Exoplanet Survey Telescope (PEST). PEST is a home observatory located near the city of Perth, Western Australia. The 1530×1020 pixel SBIG ST-8XME camera has an image scale of $1''.23 \text{ pixel}^{-1}$, resulting in a $31' \times 21'$ field of view. Image reduction and aperture photometry were performed using the C-Munipack program coupled with custom scripts. The light curve has a precision of ~ 3.0 ppt, which is easily sufficient to verify that the transit depth is consistent with the other light curves.

2.2.4. Brierfield Observatory

We observed a transit of TOI 905 on 2019 July 27 in the I band using a 0.36 m telescope (PlaneWave CDK14) at the Brierfield Observatory, a home observatory in Brierfield, New South Wales, Australia. The detector was a Moravian 16803 camera, which provided a pixel scale of $1''.47 \text{ pixel}^{-1}$. Seeing conditions were average, with some early high cloud limiting pre-ingress time. We observed a continuous transit using 137 images over 452 minutes. The images were reduced and measured as described in Section 2.2.1 with a photometric aperture of $8''.8$.

2.2.5. El Sauce

We observed the ingress and transit of TOI 905 on 2019 July 31 in the R_c band with a 0.36 m telescope (PlaneWave CDK14) at the El Sauce Observatory, located in Coquimbo Province, Chile. The detector was an SBIG STT1603-1 CCD with a pixel scale of $4''.46 \text{ pixel}^{-1}$. We acquired 186 images over 184 minutes that were processed with AIJ. Conditions were excellent, with no moon or clouds. However, the camera lost its

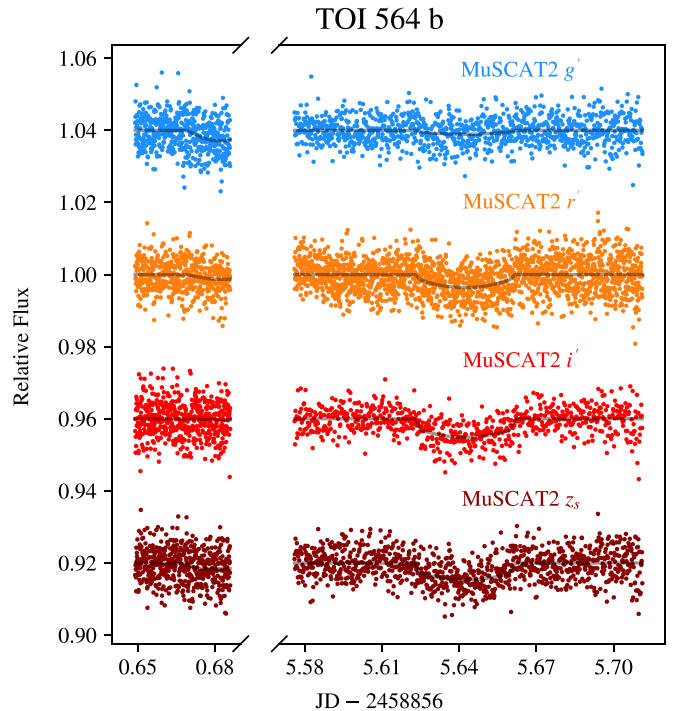


Figure 3. Two transits of TOI 564 b observed by MuSCAT2 on 2020 January 8 and 2020 January 13 (Section 2.2.6). These data were not used in the global fit. Models fitted only to these data are shown in gray.

USB connection shortly before egress, so this part of the transit was not captured in this data set.

2.2.6. MuSCAT2

We additionally observed two transits of TOI 564 b on 2020 January 8 and 2020 January 13 with the multicolor simultaneous camera MuSCAT2 (Narita et al. 2019) on the Telescopio Carlos Sanchez (TCS) located at the Teide Observatory in Tenerife, Spain. MuSCAT2 can take high-precision simultaneous multicolor photometry in the g', r', i' , and z_s bands. Data were reduced with a dedicated MuSCAT2 pipeline (Parviainen et al. 2019). The first night’s observation only covered an ingress, as the observation was interrupted by high humidity. The second night’s observation covered a full transit, and a grazing transit was clearly detected. Figure 3 shows the detrended data for both transit observations. These data were not included in the global fitting.

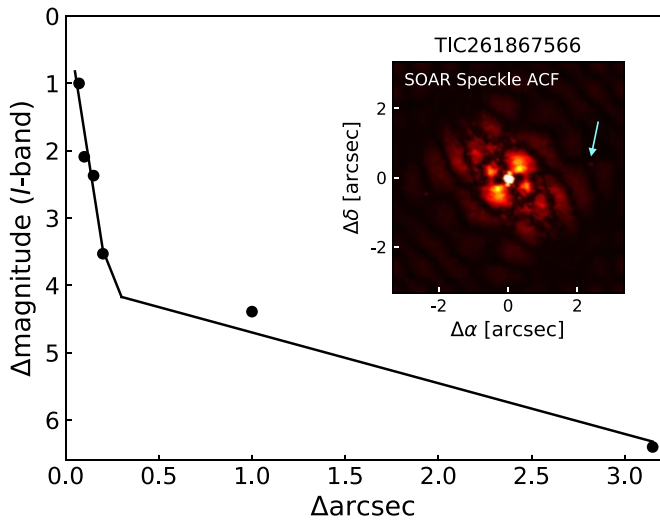


Figure 4. The HRCam *I*-band contrast curve for TOI 905 with the ACF inset. Each point gives the measured 5σ contrast at various separations from the target, with a smoothing line indicating the expected shape of the contrast curve. The cyan arrow indicates the $\Delta\text{mag} = 5.9$ companion $2''.28$ away from the primary star.

2.3. High Angular Resolution Observations

High angular resolution observations were used to check both systems for close binary companions (including background stars or bound binary companions). We found that both stars have a faint companion nearby, all located within the apertures of the available photometric observations.

2.3.1. SOAR/HRCam

On 2019 May 18, TOI 564 was observed using speckle interferometry with HRCam (Tokovinin 2018; Ziegler et al. 2020) in the *I* band on the SOAR 4.1 m telescope. The detector has a pixel scale of $15.75 \text{ mas pixel}^{-1}$, and the angular resolution was 63 mas. We rule out any companions above this limit (e.g., we can rule out a 5.1 mag companion at $>1''$ separation).

On 2019 August 12, HRCam also conducted *I*-band speckle interferometric observations of TOI 905 with an angular resolution of 71 mas. The autocorrelation function (ACF) image in Figure 4 shows the 5σ detection limit for this target. The HRCam reveals another source located $2''.28$ away from TOI 905 that is 5.9 mag fainter in the *I* band. There is no evidence that this companion is physically associated with the system.

2.3.2. Palomar 5.1 m/PHARO

On 2019 November 10, TOI 564 was observed with adaptive optics (AO) using the Palomar High Angular Resolution Observer (PHARO; Hayward et al. 2001) on the 5.1 m Hale Telescope in the *H* (continuum) and *K* (narrowband $\text{Br}\gamma$) bands. Figure 5 reveals that a stellar companion is located $0''.5$ away from the primary star, with an *H* magnitude of 13.40 ± 0.04 and a *K* magnitude of 13.18 ± 0.03 . These magnitudes and the *H* – *K* color are consistent with an early-to-mid-M dwarf binary companion with a projected separation of 100 au or a giant star 4–5 kpc distant. The former scenario is more parsimonious, and it has greater potential to create a false-positive (FP) detection (see Section 5.1.1).

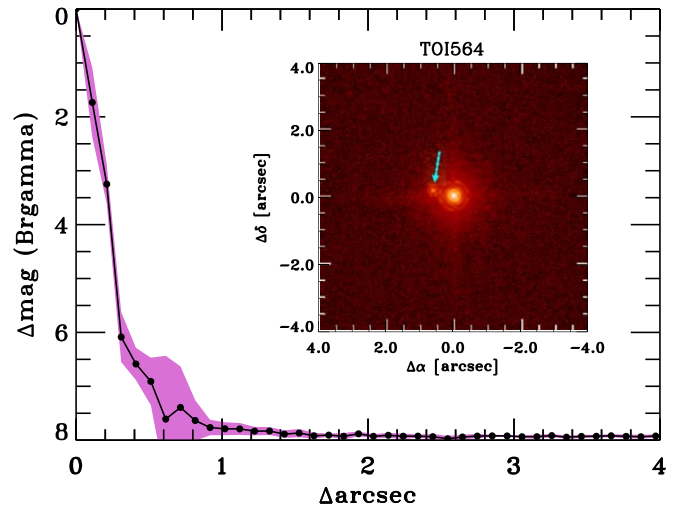


Figure 5. PHARO $\text{Br}\gamma$ (*K*-band) contrast curve for TOI 564 with AO image inset. The cyan arrow indicates a $\Delta\text{mag} = 3.53$ companion $0''.5$ away from the primary star.

2.4. Doppler Measurements

We obtained radial velocity (RV) measurements of both systems using three high-precision spectrographs. The velocities for TOI 564 (Figure 6) and TOI 905 (Figure 7) both show strong and clear Keplerian signals, which are discussed in more detail in Section 4.

2.4.1. FLWO 1.5 m/TRES

We obtained two spectra of TOI 564 with TRES (Fűrész et al. 2008) on the 1.5 m Tillinghast reflector telescope at Fred L. Whipple Observatory (FLWO) on Mount Hopkins, Arizona, on 2019 April 15 and 16. TRES is an $R \sim 44,000$ echelle spectrograph with a precision of $\sim 10\text{--}15 \text{ m s}^{-1}$. Spectra are calibrated using a pair of ThAr lamp exposures flanking each set of science exposures. Observations used exposure times of ~ 20 minutes, which yielded a signal-to-noise ratio (S/N) per resolution element of ~ 32 at 5110 \AA . TRES has an on-sky fiber radius of $1''.15$.

The reduction and analysis procedures are described in Buchhave et al. (2010). To summarize, the 2D spectra are optimally extracted and then cross-correlated order by order using the stronger of the two observations as the template. The RVs are determined from a fit to the summed cross-correlation function (CCF), and the internal errors at each epoch are estimated from the standard deviation of the RVs derived from the CCF of each order. We also track the instrumental zero-point and precision by monitoring RV standards every night, and we use this analysis to adjust the RVs and uncertainties. While the internal errors dominate for this star, we do inflate them by adding the instrumental uncertainty ($\sim 10 \text{ m s}^{-1}$) in quadrature. The RVs and uncertainties reported in Table 3 include these corrections.

2.4.2. SMARTS 1.5 m/CHIRON

We collected 10 spectra of TOI 564 with CHIRON (Tokovinin et al. 2013), a fiber-fed spectrograph on the SMARTS 1.5 m telescope at Cerro Tololo, Chile, between 2019 May 4 and 2019 June 4 and 16 spectra of TOI 905 between 2019 August 5 and 2019 August 30. The short period of both planet candidates allowed us to quickly verify that the

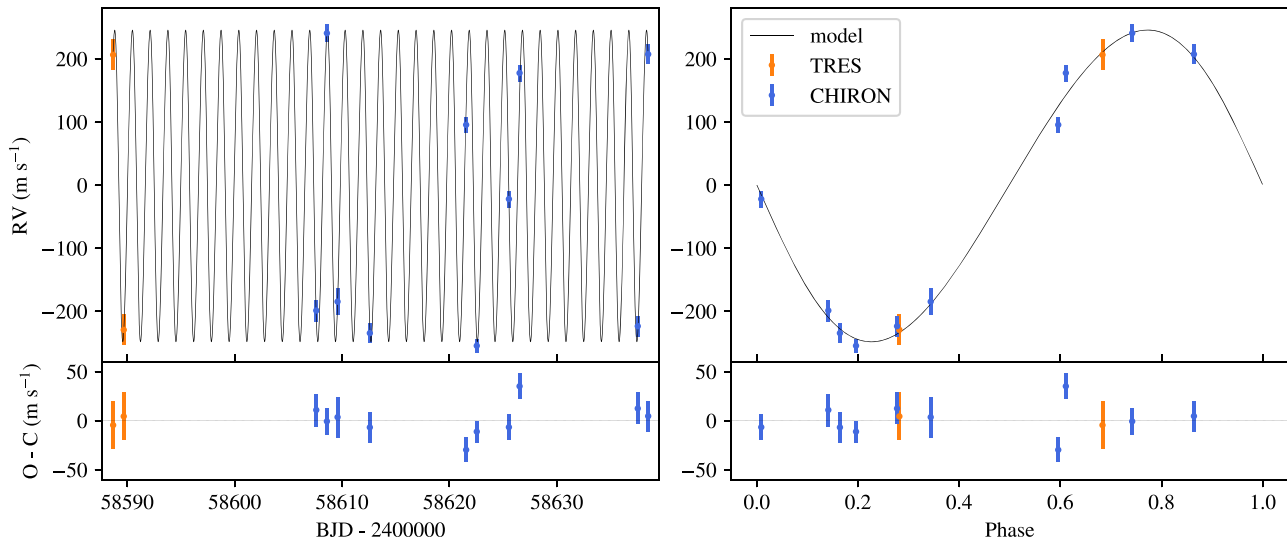


Figure 6. Left: RVs of TOI 564 as a function of time, with RVs from TRES and CHIRON plotted in orange and blue, respectively. Shown in black is the modeled RV curve based on the median posterior values for parameters derived from the global fitting given in Table 5. TRES RVs were offset to minimize the rms residual from the model determined by CHIRON data. Right: same as left panel but with RV given as a function of orbital phase. The transit is centered at phase = 0; the closest RV observation to this point did not occur during the transit.

star showed an RV signal consistent with a planetary-mass companion by observing each star near the quadrature points implied by the transit ephemerides and the assumption of a circular orbit. We then proceeded to fill out the phase curve of each planet’s orbit.

For all observations, we used CHIRON’s $R = 80,000$ slicer mode, which provides substantially higher instrumental throughput when compared to the slit or narrow slit modes (the relative efficiencies of the modes are 0.82, 0.25, and 0.11, respectively; Tokovinin et al. 2013). In addition, we did not use the iodine cell, which would have absorbed about half of the stellar light in the $\sim 5000\text{--}6100$ Å region. Each observation used an exposure time of 25 minutes, which provided a typical S/N per resolution element of ~ 40 at 5500 Å. The on-sky fiber radius of CHIRON is $1''.35$.

The RVs were derived closely following the procedure described in Jones et al. (2017) and Wang et al. (2019). Briefly, we first built a template by stacking the individual CHIRON spectra, after shifting all of them to a common rest frame. We then computed the CCF between each observed spectrum and the template. The CCF was then fitted with a Gaussian function plus a linear trend. The velocity corresponding to the maximum of the Gaussian fit corresponds to the observed RV. We applied this method to a total of 33 orders, covering the wavelength range of $\sim 4700\text{--}6500$ Å. Since CHIRON is not equipped with a simultaneous calibration fiber, we obtained a ThAr lamp immediately before each science observation. The CHIRON pipeline therefore recomputes a new wavelength solution from this calibration observation, thus correcting for the instrumental drift. Using this method, we achieve a long-term stability better than 10 m s^{-1} , which has been tested using RV standard stars. The final RV at each epoch is obtained from the median in the individual order velocities after applying a 3σ rejection method. The corresponding uncertainty is computed from the error in the mean of the nonrejected velocities (see more details in Jones et al. 2017). The typical RV error found was about 15 m s^{-1} . Finally, we also computed the bisector inverse slope (BIS) and FWHM of the CCF. The full results of the CCF

analysis are given in Table 3, including the BIS and FWHM diagnostics.

2.4.3. ESO 3.6 m/HARPS

We collected two spectra of TOI 905 with the High Accuracy Radial velocity Planet Searcher (HARPS; Mayor et al. 2003) at the ESO 3.6 m telescope. HARPS has a spectral resolution of $R = 115,000$ and a fiber with an on-sky radius of $0''.5$. Exposure times were 25 minutes, achieving $S/N \sim 42$ at 5500 Å.

Our motivation in collecting HARPS spectra was to test whether the semiamplitude of the signal was consistent between HARPS and CHIRON, which have sky fibers of $0''.5$ and $1''.35$, respectively. If there is potential RV contamination from the nearby star $2''.28$ away (Section 2.3.1), then the Doppler semiamplitude should be different between the instruments. Figure 7 shows that when the HARPS RVs are offset to match CHIRON, they agree closely.

3. Host Star Characterization

It is well understood that when the transit and RV techniques are used for planet characterization, we can only know the planet as well as we know the star. We derived physical and atmospheric parameters for TOI 564 and TOI 905 using several independent methodologies and data sets that are described in the following subsections (the stellar parameters determined by EXOFASTv2 are described later in Section 4).

We find that among the values probed by multiple methods, there is generally agreement within $1\sigma\text{--}2\sigma$, giving us greater confidence in their collective veracity. Both stars are G-type main-sequence stars, which are roughly Sun-like in their mass, radius, and temperature. Both stars are metal-rich. A summary of the parameters derived is shown in Table 4.

3.1. Results from FLWO 1.5 m/TRES

We derived spectral parameters from the TRES spectra of TOI 564 using the spectral parameter classification (SPC) tool (Buchhave et al. 2012). It cross-correlates the observed

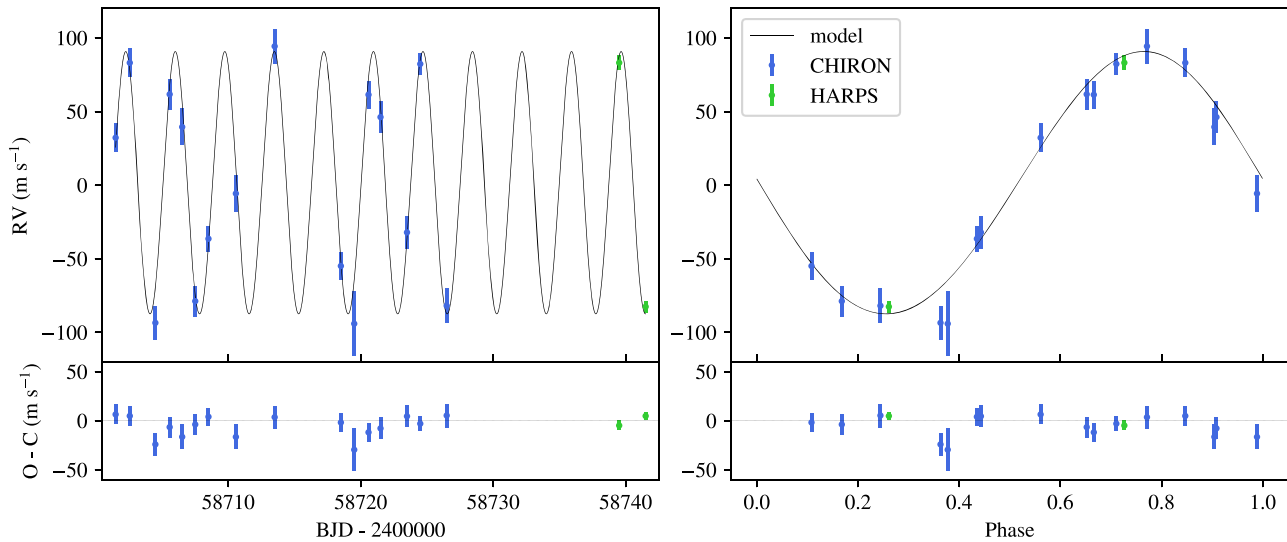


Figure 7. Left: RVs of TOI 905 as a function of time, with RVs from CHIRON and HARPS plotted in blue and green, respectively. Shown in black is the modeled RV curve based on the median posterior values for parameters derived from the global fitting given in Table 5. HARPS RVs were offset to minimize the rms residual from the model determined by CHIRON data. Right: same as left panel but with RV given as a function of orbital phase. The transit occurs at phase = 0.

spectrum against a grid of synthetic spectra based on Kurucz atmospheric models (Kurucz 1993). Here T_{eff} , $\log g_*$, $[\text{Fe}/\text{H}]$, and $V \sin i$ are allowed to vary as free parameters. We find that $T_{\text{eff}} = 5666 \pm 50$ K, $\log g_* = 4.41 \pm 0.10$, $[\text{Fe}/\text{H}] = 0.15 \pm 0.08$, and $V \sin i = 3.54 \pm 0.5$ km s $^{-1}$.

3.2. Results from SMARTS 1.5 m/CHIRON

We derive the atmospheric parameters of both TOI 564 and TOI 905 following the method presented in Jones et al. (2011) and Wang et al. (2019). We used the CHIRON template (see Section 2.4) to measure the equivalent widths (EWs) of a total of 110 Fe I and 20 Fe II lines in the weak-line regime ($\text{EW} < 150$ Å). The EWs were measured after fitting the local continuum using the ARES2 v2 automatic tool (Sousa et al. 2015).

We then solved the radiative transfer equation by imposing local excitation and ionization equilibrium (Boltzmann and Saha equations, respectively) and assuming a solar metal content distribution. For this, we used the MOOG code (Snedden 1973) along with the Kurucz (1993) stellar atmosphere models. For models with different T_{eff} , $\log g_*$, and $[\text{Fe}/\text{H}]$, we iterate until no dependence between the excitation potential and wavelength of the individual lines with the model abundance is found and with the constraint that the model abundance is the same for both the Fe I and Fe II lines. We note that the microturbulence velocity (v_t) is a free parameter in the fit. Using this method, we obtained the following atmospheric parameters for TOI 564: $T_{\text{eff}} = 5780 \pm 100$ K, $\log g_* = 4.23 \pm 0.20$ dex, $[\text{Fe}/\text{H}] = 0.34 \pm 0.20$, and $v_t = 0.75 \pm 0.10$ km s $^{-1}$. For TOI 905, we found $T_{\text{eff}} = 5300 \pm 100$ K, $\log g_* = 3.94 \pm 0.20$ dex, and $[\text{Fe}/\text{H}] = 0.20 \pm 0.10$.

We adopted a value of $A_V = 0.10 \pm 0.10$ for the interstellar reddening to derive corrected visual apparent magnitudes. We also correct the Gaia parallax by a systematic offset of 82 ± 32 μas (Stassun & Torres 2018) to obtain $\varpi = 5.0638 \pm 0.04738$ and $6.66^{+0.32}_{-0.30}$ for TOI 564 and TOI 905, respectively. Using the bolometric corrections presented in Alonso et al. (1999), we calculate a stellar luminosity of $L_* = 1.06 \pm 0.11 L_\odot$. Finally, by comparing L_* , T_{eff} , and

$[\text{Fe}/\text{H}]$ with the PARSEC evolutionary tracks (Bressan et al. 2012), we derived a stellar mass and radius of $1.1 \pm 0.1 M_\odot$ and $1.04 \pm 0.05 R_\odot$, respectively, for TOI 564 and $0.85 \pm 0.10 M_\odot$ and $1.14 \pm 0.03 R_\odot$ for TOI 905.

3.3. Results from Independent SED Fitting

Although we will compute stellar parameters based on the broadband spectral energy distribution (SED) in a global analysis using EXOFASTv2 (see Section 4), we also perform a separate SED analysis as an independent check on the derived stellar parameters. Here we use the SED together with the Gaia DR2 parallax in order to determine an empirical measurement of the stellar radius following the procedures described in Stassun & Torres (2016) and Stassun et al. (2017, 2018a). We pulled the $B_T V_T$ magnitudes from Tycho-2, the $B V g r i$ magnitudes from APASS, the $J H K_S$ magnitudes from the Two Micron All Sky Survey (2MASS), the W1–W4 magnitudes from the Wide-field Infrared Survey Explorer (WISE), the G magnitude from Gaia, and the near-UV (NUV) magnitude from the Galaxy Evolution Explorer. Together, the available photometry spans the full stellar SED over the wavelength range 0.2–22 μm for TOI 564 and 0.4–22 μm for TOI 905.

We performed a fit using Kurucz stellar atmosphere models. The priors on effective temperature (T_{eff}), surface gravity ($\log g_*$), and metallicity ($[\text{Fe}/\text{H}]$) were from spectroscopically determined values for TOI 564 and from the values provided in the TIC (Stassun et al. 2018b) for TOI 905. The remaining free parameter is the extinction (A_V), which we restricted to the maximum line-of-sight value from the dust maps of Schlegel et al. (1998). The resulting fits for TOI 564 and TOI 905 are excellent (see Figure 8 and Figure 9). The reduced χ^2 values for the TOI 905 fit is 1.3, while the reduced χ^2 for TOI 564 improves from 3.8 to 1.6 when the NUV point is excluded; this NUV excess suggests mild chromospheric activity. The best-fit extinction is $A_V = 0.03^{+0.11}_{-0.03}$ for TOI 564 and $A_V = 0.06 \pm 0.03$ for TOI 905. Integrating the (unreddened) model SED gives a bolometric flux at Earth of $F_{\text{bol}} = 9.04 \pm 0.32 \times 10^{-10}$ erg s cm $^{-2}$ for TOI 564 and

Table 3
RV Measurements

BJD ^a –2,400,000	RV ^b (m s ⁻¹)	σ_{RV} (m s ⁻¹)	BIS (m s ⁻¹)	σ_{BIS} (m s ⁻¹)	FWHM (km s ⁻¹)	σ_{FWHM} (km s ⁻¹)	S/N ^c	Target	Instrument
58,588.6801	413.0	24.4	6.9	10.2	31.0	TOI 564	TRES
58,589.6683	-22.8	24.4	-6.9	10.2	34.2	TOI 564	TRES
58,607.5990	-198.7	16.7	13.7	10.5	10.124	0.153	37.1	TOI 564	CHIRON
58,608.5907	240.8	13.6	8.6	9.1	10.441	0.118	47.6	TOI 564	CHIRON
58,609.5843	-184.6	20.8	27.4	12.9	9.501	0.163	30.9	TOI 564	CHIRON
58,612.5903	-234.5	15.3	-12.0	15.2	10.162	0.129	38.7	TOI 564	CHIRON
58,621.5585	95.6	12.3	12.0	10.2	10.088	0.116	39.8	TOI 564	CHIRON
58,622.5497	-254.5	10.9	13.7	9.6	10.107	0.122	39.4	TOI 564	CHIRON
58,625.5427	-22.0	13.2	30.9	10.9	10.243	0.128	38.4	TOI 564	CHIRON
58,626.5368	177.7	13.1	24.0	8.1	10.405	0.125	48.5	TOI 564	CHIRON
58,637.5439	-223.5	15.9	18.9	13.5	10.241	0.134	43.0	TOI 564	CHIRON
58,638.5128	207.4	15.6	22.3	15.9	10.195	0.112	39.9	TOI 564	CHIRON
58,701.4994	32.2	9.7	1.3	16.5	9.953	0.073	46.8	TOI 905	CHIRON
58,702.5685	83.1	9.7	-2.6	14.1	9.885	0.079	42.2	TOI 905	CHIRON
58,704.4989	-93.5	11.3	-16.7	19.2	9.747	0.100	36.3	TOI 905	CHIRON
58,705.5794	61.7	10.3	-14.1	18.9	9.864	0.094	41.1	TOI 905	CHIRON
58,706.5228	39.5	12.3	-7.7	22.4	9.842	0.087	38.1	TOI 905	CHIRON
58,707.5088	-78.8	10.2	-18.0	13.6	9.804	0.085	39.8	TOI 905	CHIRON
58,708.5073	-36.4	8.8	-27.0	16.4	9.860	0.087	44.7	TOI 905	CHIRON
58,710.5776	-5.7	12.4	0.0	20.4	9.766	0.096	38.8	TOI 905	CHIRON
58,713.5038	94.3	11.6	10.3	11.1	9.917	0.088	44.4	TOI 905	CHIRON
58,718.5033	-54.9	9.4	-12.9	16.5	9.984	0.083	45.8	TOI 905	CHIRON
58,719.5102	-94.1	21.8	-78.4	31.2	9.598	0.108	28.9	TOI 905	CHIRON
58,720.5899	61.4	9.4	6.4	16.8	9.951	0.091	44.6	TOI 905	CHIRON
58,721.4963	46.2	10.7	1.3	14.9	9.937	0.081	44.1	TOI 905	CHIRON
58,723.4948	-32.1	10.9	-12.9	25.0	9.826	0.090	38.9	TOI 905	CHIRON
58,724.4959	82.3	7.3	9.0	14.4	9.968	0.087	45.4	TOI 905	CHIRON
58,726.4917	-81.9	11.8	38.6	20.1	9.871	0.085	40.2	TOI 905	CHIRON
58,739.513	83.1	4.845	43.4	...	6.664	...	39.9	TOI 905	HARPS
58,741.512	-82.5	4.054	15.9	...	6.673	...	44.5	TOI 905	HARPS

Notes.^a Times are reported according to the BJD at the UTC time at the midpoint of each exposure.^b CHIRON RVs are reported with an arbitrary zero-point. The zero-points for the TRES and HARPS RVs were each chosen to minimize the least-squares distance from the RV model for the target system based on the global analysis performed on the CHIRON RVs and photometry.^c S/N per resolution element, reported at 5110 Å for TRES and 5500 Å for CHIRON and HARPS.

$F_{bol} = 9.13 \pm 0.21 \times 10^{-10}$ erg s⁻¹ cm⁻² for TOI 905. Taking the F_{bol} and T_{eff} together with the Gaia DR2 parallax, adjusted by +0.08 mas to account for the systematic offset reported by Stassun & Torres (2018), gives the stellar radius as $R = 1.092 \pm 0.020 R_{\odot}$ for TOI 564 and $0.964 \pm 0.052 R_{\odot}$ for TOI 905. Finally, estimating the stellar mass from the empirical relations of Torres et al. (2010) gives $M = 1.06 \pm 0.06 M_{\odot}$, which, with the radius, gives a mean stellar density $\rho = 1.15 \pm 0.12$ g cm⁻³ for TOI 564. We find $1.15 \pm 0.07 M_{\odot}$ and $\rho = 1.82 \pm 0.31$ g cm⁻³ for TOI 905.

4. Planetary System Parameters from Global Analysis

We model planetary system and stellar parameters as in Wang et al. (2019) using EXOFASTv2⁴⁹ (Eastman et al. 2013; Eastman 2017; Eastman et al. 2019), a fast and powerful exoplanetary fitting suite. We performed a global simultaneous analysis of both systems using light curves from TESS, LCOCTIO, PEST, LCO-SSO, Brierfield, and El Sauce; RVs from CHIRON; and stellar SEDs. We did not include the MLAO *B*-band light curve for TOI 564 because of its lower precision compared to the LCO-SSO *B*-band light curve. We also did not

include the two TRES or the two HARPS RVs, which, on their own, were not informative enough to justify introducing an additional two degrees of freedom to the fitting (namely instrumental offset and instrumental jitter); nevertheless, we note that each of these pairs of RVs were consistent with the CHIRON RVs in both systems.

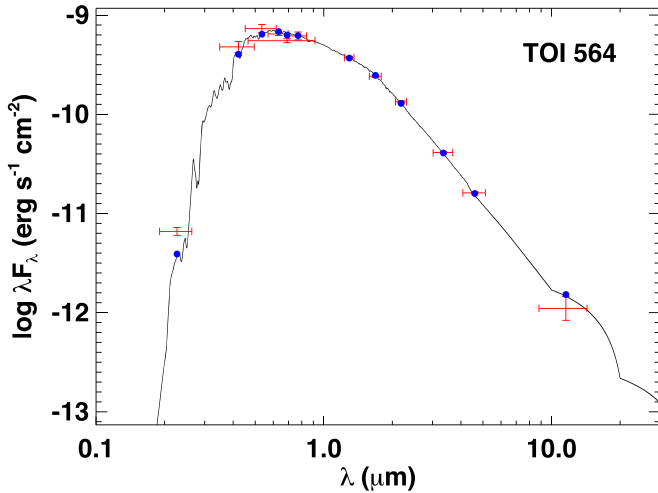
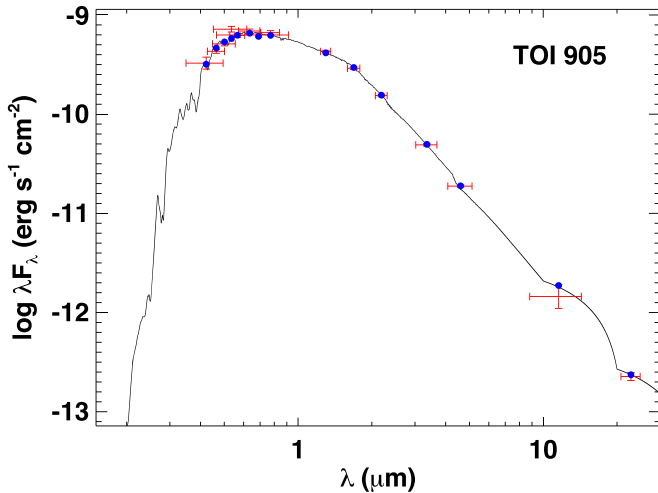
During the global fitting, we applied the quadratic limb-darkening law and performed a coefficients fit with a TESS-band prior based on the relation of stellar parameters ($\log g_{*}$, T_{eff} , and [Fe/H]) and coefficients (Claret 2018). The corrected Gaia parallax for each target (Section 3.2) is adopted as the Gaussian prior imposed on the Gaia DR2 parallaxes. An upper limit is imposed on the *V*-band extinction of 0.14 from Schlafly & Finkbeiner (2011).

To constrain each SED, we utilized the photometry from Tycho (Høg et al. 2000), 2MASS *JHK* (Cutri et al. 2003), AllWISE (Cutri et al. 2013), and Gaia DR2 (Gaia Collaboration et al. 2018); these magnitudes are given in Table 1. With the initial value of T_{eff} (5780 ± 100 and 5300 ± 100 K for TOI 564 and TOI 905, respectively) derived from Section 3.2, we utilized the available SED and the MIST stellar evolutionary models (Choi et al. 2016; Dotter 2016) to further constrain the stellar parameters.

⁴⁹ <https://github.com/jdeast/EXOFASTv2>

Table 4
Stellar Parameters

Parameter	FLWO 1.5 m/TRES	SMARTS 1.5 m/CHIRON	SED (Stassun)	SED (EXOFASTv2)
TOI 564				
M_* (M_\odot)	...	1.1 ± 0.1	1.06 ± 0.06	$0.998^{+0.068}_{-0.057}$
R_* (R_\odot)	...	1.04 ± 0.05	1.092 ± 0.020	1.088 ± 0.014
L_* (L_\odot)	...	1.06 ± 0.11	...	$1.078^{+0.028}_{-0.030}$
T_{eff} (K)	5666 ± 50	5780 ± 100	...	5640^{+34}_{-37}
$\log g_*$ (cgs)	4.41 ± 0.10	4.23 ± 0.20	...	$4.364^{+0.032}_{-0.028}$
$V \sin i$ (km s^{-1})	3.54 ± 0.5
[Fe/H] (dex)	0.15 ± 0.08	0.34 ± 0.20	...	$0.143^{+0.076}_{-0.078}$
Age (Gyr)	$7.3^{+3.5}_{-3.6}$
TOI 905				
M_* (M_\odot)	...	0.85 ± 0.10	1.15 ± 0.07	$0.968^{+0.061}_{-0.068}$
R_* (R_\odot)	...	1.14 ± 0.03	0.964 ± 0.052	$0.918^{+0.038}_{-0.036}$
L_* (L_\odot)	...	0.93 ± 0.05	...	$0.730^{+0.12}_{-0.095}$
T_{eff} (K)	...	5300 ± 100	...	5570^{+150}_{-140}
$\log g_*$ (cgs)	...	3.94 ± 0.20	...	$4.498^{+0.025}_{-0.027}$
$V \sin i$ (km s^{-1})
[Fe/H] (dex)	...	0.20 ± 0.10	...	$0.14^{+0.22}_{-0.18}$
Age (Gyr)	$3.4^{+3.8}_{-2.3}$

**Figure 8.** The SED of TOI 564. Red symbols represent the observed photometric measurements, where the horizontal bars represent the effective width of the passband. Blue symbols are the model fluxes from the best-fit Kurucz atmosphere model (black).**Figure 9.** Same as Figure 8 but for TOI 905.

We began the fit with relatively standard hot Jupiter starting conditions, but, as suggested by Eastman et al. (2019), we iterated with relatively short MCMC runs with parallel tempering enabled to refine the starting conditions and ensure that the AMOEBA optimizer could find a good solution to all constraints simultaneously. This is not strictly required but can dramatically improve the efficiency of EXOFASTv2. Once we found a good solution, we ran a final fit until the standard criteria (both the number of independent draws being greater than 1000 and a Gelman–Rubin statistic of less than 1.01 for all parameters) were satisfied six consecutive times, indicating that the chains were considered to be well mixed (Eastman et al. 2013).

Table 5 summarizes the relevant parameters reported by EXOFASTv2, with median values and 68% confidence intervals (CIs) for each posterior. It is found that TOI 564 is Sun-like, with a mass of $0.998^{+0.068}_{-0.057} M_\odot$, radius of $1.088 \pm 0.014 R_\odot$, and T_{eff} of 5640^{+34}_{-37} K; TOI 905 is slightly smaller, with a mass of $0.968^{+0.061}_{-0.068} M_\odot$, radius of $0.918^{+0.038}_{-0.036} R_\odot$, and T_{eff} of 5570^{+150}_{-140} K. The two stars are each metal-rich, with $[\text{Fe}/\text{H}] = 0.143^{+0.076}_{-0.078}$ and $0.14^{+0.22}_{-0.18}$ dex, respectively, which is consistent with our understanding of hot Jupiter host stars (Fischer & Valenti 2005).

The masses of both planets are determined from the CHIRON RVs and the modeled inclinations. The object TOI 564 b has a mass of $1.463^{+0.10}_{-0.096} M_J$, and TOI 905 b has a mass of $0.667^{+0.042}_{-0.041} M_J$. The RV curves corresponding to the median posterior values for the relevant orbital and planetary parameters are shown in Figures 6 and 7 in black.

The transit models based on the median posterior values for each planet and photometric band are plotted in Figures 1 and 2. EXOFASTv2 finds a median radius and 68% CI of TOI 905 b of $1.171^{+0.053}_{-0.051} R_J$. The radius of TOI 564 b is far more difficult to constrain; we find a median and 68% CI of $1.02^{+0.71}_{-0.29} R_J$. This value is very sensitive to small changes in the impact parameter, which we determine to be $0.994^{+0.083}_{-0.049}$ with an inclination of $78.38^{+0.71}_{-0.85}^\circ$. This high impact parameter corresponds to a grazing transit scenario and creates a tricky interplay between the modeled R_p and b .

Table 5
Median Values and 68% CIs for the TOI 564 and TOI 905 Planetary Systems

Parameter	Units	Values			
Stellar Parameters		TOI 564	TOI 905		
M_*	Mass (M_\odot)	$0.998^{+0.068}_{-0.057}$	$0.968^{+0.061}_{-0.068}$		
R_*	Radius (R_\odot)	1.088 ± 0.014	$0.918^{+0.038}_{-0.036}$		
L_*	Luminosity (L_\odot)	$1.078^{+0.028}_{-0.030}$	$0.730^{+0.12}_{-0.095}$		
ρ_*	Density (cgs)	$1.095^{+0.090}_{-0.075}$	1.76 ± 0.16		
$\log g$	Surface gravity (cgs)	$4.364^{+0.032}_{-0.028}$	$4.498^{+0.025}_{-0.027}$		
T_{eff}	Effective temperature (K)	5640^{+34}_{-37}	5570^{+150}_{-140}		
[Fe/H]	Metallicity (dex)	$0.143^{+0.076}_{-0.078}$	$0.14^{+0.22}_{-0.18}$		
[Fe/H] ₀	Initial metallicity	$0.165^{+0.069}_{-0.072}$	$0.12^{+0.19}_{-0.16}$		
Age	Age (Gyr)	$7.3^{+3.6}_{-3.5}$	$3.4^{+3.8}_{-2.3}$		
A_V	V-band extinction (mag)	$0.108^{+0.021}_{-0.033}$	0.23 ± 0.12		
σ_{SED}	SED photometry error scaling	$1.27^{+0.42}_{-0.27}$	$1.54^{+0.49}_{-0.32}$		
ϖ	Parallax (mas)	5.067 ± 0.046	$6.66^{+0.32}_{-0.30}$		
d	Distance (pc)	197.4 ± 1.8	$150.2^{+7.2}_{-6.9}$		
Planetary Parameters		TOI 564 b	TOI 905 b		
P	Period (days)	1.651144 ± 0.000018	3.739494 ± 0.000038		
R_P	Radius (R_J)	$1.02^{+0.71}_{-0.29}$	$1.171^{+0.053}_{-0.051}$		
M_P	Mass (M_J)	$1.463^{+0.10}_{-0.096}$	$0.667^{+0.042}_{-0.041}$		
ρ_P	Density (cgs)	$1.7^{+3.1}_{-1.4}$	$0.515^{+0.063}_{-0.057}$		
T_C	Time of conjunction (BJD _{TDB})	$2458,518.203,81^{+0.00057}_{-0.00058}$	$2,458,628.35101 \pm 0.00026$		
T_0	Optimal conjunction time (BJD _{TDB})	$2458,549.575,54^{+0.00045}_{-0.00046}$	$2,458,643.30898 \pm 0.00020$		
a	Semimajor axis (au)	$0.02734^{+0.00061}_{-0.00053}$	$0.04666^{+0.00096}_{-0.0011}$		
i	Inclination (deg)	$78.38^{+0.71}_{-0.85}$	$85.68^{+0.22}_{-0.26}$		
e	Eccentricity	$0.072^{+0.083}_{-0.050}$	$0.024^{+0.025}_{-0.017}$		
ω_*	Argument of periastron (deg)	94^{+32}_{-35}	39^{+61}_{-82}		
K	RV semi-amplitude (m s^{-1})	247 ± 13	$89.1^{+3.8}_{-3.6}$		
T_{eq}	Equilibrium temperature (K)	1714^{+20}_{-21}	1192^{+39}_{-36}		
τ_{circ}	Tidal circularization timescale (Gyr)	$0.043^{+0.20}_{-0.040}$	$0.323^{+0.063}_{-0.054}$		
δ	Transit depth (fraction)	$0.0092^{+0.017}_{-0.0045}$	$0.01718^{+0.00032}_{-0.00030}$		
Depth	Flux decrement at mid-transit	$0.00484^{+0.00039}_{-0.00047}$	$0.01718^{+0.00032}_{-0.00030}$		
b	Transit impact parameter	$0.994^{+0.083}_{-0.049}$	$0.816^{+0.010}_{-0.012}$		
τ	Ingress/egress transit duration (days)	$0.02139^{+0.00062}_{-0.00077}$	$0.0278^{+0.012}_{-0.0038}$		
T_{14}	Total transit duration (days)	$0.0428^{+0.0012}_{-0.0013}$	$0.0845^{+0.0011}_{-0.0015}$		
b_S	Eclipse impact parameter	$1.152^{+0.14}_{-0.089}$	$0.827^{+0.047}_{-0.031}$		
τ_S	Ingress/egress eclipse duration (days)	$0.000^{+0.021}_{-0.00}$	$0.0278^{+0.012}_{-0.0038}$		
$T_{S,14}$	Total eclipse duration (days)	$0.000^{+0.041}_{-0.00}$	$0.0845^{+0.0011}_{-0.0015}$		
$\log g_P$	Surface gravity	$3.55^{+0.30}_{-0.46}$	3.081 ± 0.035		
$\langle F \rangle$	Incident flux ($10^9 \text{ erg s}^{-1} \text{ cm}^{-2}$)	$1.937^{+0.099}_{-0.11}$	$0.458^{+0.063}_{-0.052}$		
T_P	Time of periastron (BJD _{TDB})	$2458,516.57^{+0.13}_{-0.14}$	$2458,627.86^{+0.60}_{-0.85}$		
T_S	Time of eclipse (BJD _{TDB})	$2458,517.374^{+0.028}_{-0.036}$	$2458,630.245^{+0.049}_{-0.031}$		
T_A	Time of ascending node (BJD _{TDB})	$2458,517.822^{+0.044}_{-0.030}$	$2458,627.436^{+0.046}_{-0.026}$		
T_D	Time of descending node (BJD _{TDB})	$2458,518.580^{+0.036}_{-0.050}$	$2458,629.288^{+0.032}_{-0.029}$		
$e \cos \omega_*$...	$-0.004^{+0.026}_{-0.033}$	$0.010^{+0.020}_{-0.013}$		
$e \sin \omega_*$...	$0.063^{+0.086}_{-0.058}$	$0.006^{+0.028}_{-0.016}$		
d/R_*	Separation at mid-transit	$5.05^{+0.33}_{-0.46}$	$10.85^{+0.47}_{-0.59}$		
Telescope Parameters		CHIRON (TOI 564)	CHIRON (TOI 905)		
γ_{rel}	Relative RV offset (m/s)	22 ± 11	$-36.2^{+2.7}_{-2.9}$		
σ_J	RV jitter (m/s)	$25.9^{+17}_{-9.7}$	$2.0^{+6.8}_{-2.0}$		
σ_J^2	RV jitter variance	670^{+1100}_{-410}	3^{+73}_{-38}		
Wavelength Parameters for TOI 564		TESS	LCO-SSO (B)	PEST (V)	LCO-CTIO (z')
u_1	Linear limb-darkening coeff.	$0.370^{+0.045}_{-0.046}$	0.664 ± 0.047	0.488 ± 0.050	0.267 ± 0.047
u_2	Quadratic limb-darkening coeff.	$0.301^{+0.046}_{-0.047}$	0.079 ± 0.048	0.220 ± 0.050	0.265 ± 0.048
Wavelength Parameters for TOI 905		TESS	LCO-SSO (G)	El Sauce (R_c)	Brierfield (I)
u_1	Linear limb-darkening coeff.	$0.345^{+0.064}_{-0.055}$	$0.637^{+0.066}_{-0.067}$	$0.424^{+0.059}_{-0.060}$	$0.315^{+0.055}_{-0.056}$
u_2	Quadratic limb-darkening coeff.	$0.263^{+0.050}_{-0.049}$	$0.153^{+0.062}_{-0.061}$	$0.262^{+0.053}_{-0.052}$	0.253 ± 0.051
Transit Parameters for TOI 564		TESS	LCO-SSO (B)	PEST (V)	LCO-CTIO (z')
σ^2	Added variance	$0.000000010 \pm 0.000000024$	$0.00000091^{+0.00000025}_{-0.00000021}$	$0.0000010^{+0.00000015}_{-0.00000012}$	$0.00000052^{+0.00000016}_{-0.00000014}$

Table 5
(Continued)

Parameter	Units	Values			
F_0	Baseline flux	$1.000011^{+0.000012}_{-0.000013}$	1.00070 ± 0.00022	0.99954 ± 0.00062	0.99994 ± 0.00019
M_0	Multiplicative detrending coeff.	–	0.00212 ± 0.00049	-0.0008 ± 0.0013	$-0.00027^{+0.00039}_{-0.00040}$
Transit Parameters for TOI 905		TESS	LCO-SSO (G)	El Sauce (R_c)	Brierfield (I)
σ^2	Added variance	$0.000000004 \pm 0.000000032$	$0.0000064^{+0.0000015}_{-0.0000013}$	$0.0000083^{+0.0000012}_{-0.0000010}$	$0.0000207^{+0.0000034}_{-0.0000029}$
F_0	Baseline flux	1.000002 ± 0.000013	0.99993 ± 0.00031	$1.00112^{+0.00028}_{-0.00027}$	1.00022 ± 0.00044

The uncertainties in the radius of TOI 564 b are compounded in the median and 68% CI of the bulk density estimate of $1.7^{+3.1}_{-1.4} \text{ g cm}^{-3}$. The density of TOI 905 b is more precisely determined to be $0.515^{+0.063}_{-0.057} \text{ g cm}^{-3}$. We find that the eccentricity is consistent with zero, with a median value and 68% CI of $0.072^{+0.083}_{-0.050}$. Indeed, a circular orbit is to be expected for this planet based on the rapid tidal circulation timescale (as computed by Adams & Laughlin 2006 with $Q_* = 10^6$) of $0.043^{+0.20}_{-0.040}$ Gyr, which is very short compared to the stellar age of $7.3^{+3.6}_{-3.5}$ Gyr. Also, TOI 905 b has an eccentricity that is consistent with a circular orbit: $0.024^{+0.025}_{-0.017}$. The tidal circularization timescale for this planet is $0.323^{+0.063}_{-0.054}$ Gyr.

5. Discussion

5.1. False-positive Scenarios

A variety of FP scenarios can result in spurious claims of planet detections. For instance, background eclipsing binaries (BEBs) or nearby eclipsing binaries (NEBs) can masquerade as giant planets in transit and RV data; these marginally resolved double-lined binaries can cause RV-correlated CCF variations while producing a diluted transit signal (e.g., Torres et al. 2004; Collins et al. 2018). We should be especially wary of these scenarios given that nearby stars were detected in proximity to both TOI 564 and TOI 905.

Here we explicitly discuss several tests for FP scenarios. Taken together, we find that the lines of evidence collectively demonstrate the planetary nature of these bodies.

5.1.1. Rejecting FP Scenarios for TOI 564 b

We examined the BIS and FWHM for possible linear correlations with the RVs using the Pearson correlation coefficient, ρ . We calculated ρ over 100,000 realizations of the data resampled from a bivariate normal distribution using the 1σ errors in both quantities. The results are shown in orange in Figure 10. Here TOI 564 shows no statistically significant correlation between BIS and RV, but the zero-correlation case for FWHM and RV is excluded with high confidence. This correlation is potentially concerning.

However, we believe that the correlation is better explained as a manifestation of systematic errors in our reduction pipeline that increase with low S/N. The correlations between the CCF and S/N are plotted in blue in Figure 10, and in the FWHM case, we see that the correlation with S/N is much tighter than with RV. In Section 5.1.2 we also discuss an independent reduction using TODCOR for TOI 905, and the results support our hypothesis that the correlation is merely a result of our pipeline not handling low-S/N cases well when deriving CCF moments.

The apparent grazing transit of TOI 564, combined with the existence of a likely M-dwarf companion in the system, raises

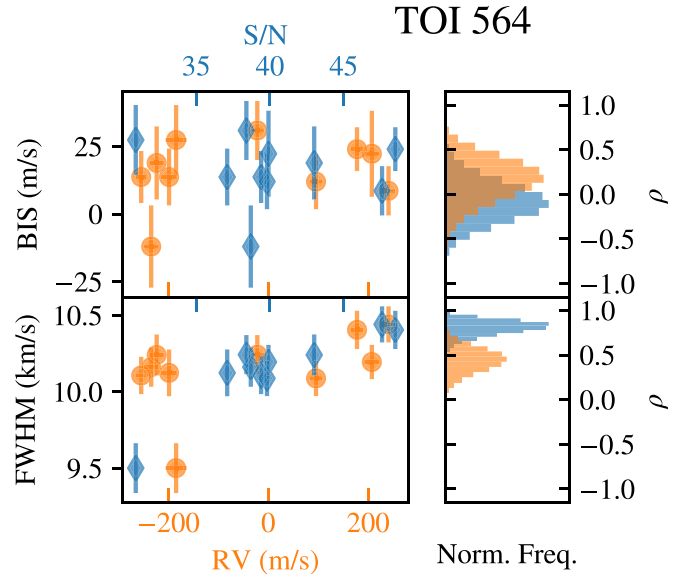


Figure 10. The CCF correlations for the CHIRON observations of TOI 564. Left: BIS (top) and FWHM (bottom) of the CCF plotted vs. both RV (orange circles) and S/N (blue diamonds). Right: histograms of the Pearson correlation coefficient (ρ) values between either BIS (top) or FWHM (bottom) vs. RV (orange) or S/N (blue), based on a resampling of the data on the left.

the possibility that the system may consist of a close M-dwarf binary pair that orbits the G star in a hierarchical triple system. In this scenario, an eclipse of the M-dwarf pair would be contaminated by the bright G star, leading to a spurious planetary transit signal, and the RVs of the system would similarly consist of high-amplitude RVs from the M-dwarf pair that are diluted by the G star.

The agreement of the 1.65 day period between the transit and RV observations rules out a mutual-eclipse scenario in a hypothetical M-dwarf pair; such a binary must only experience one eclipse per orbit. A single-eclipse orbit necessitates an orbit that has nonzero eccentricity. The RVs for this system constrain the eccentricity to $0.072^{+0.083}_{-0.050}$.

We simulated this geometry, assuming the two M dwarfs were each $0.3 M_\odot$ and $0.3 R_\odot$. The semimajor axis is therefore 0.0231 au. We find that an inclination of $82^\circ.5 < i < 83^\circ.5$ is required to produce exactly one eclipse in this scenario. Although possible, it would be unlikely a priori to find a two-body system that falls within such tight inclination bounds.

Furthermore, in this hierarchical triple-system scenario, an eclipse of an M dwarf would produce transits that are deeper in redder wavelengths, in accordance with the cool stars' colors. A typical M3 star has $B - V = 1.5$, compared to the primary star's measured $B - V$ value of 0.77. This color difference between the two spectral types corresponds to a factor of ~ 2 difference in the expected transit depths between B and V if the M dwarf is being eclipsed. Instead, we find that there is only an

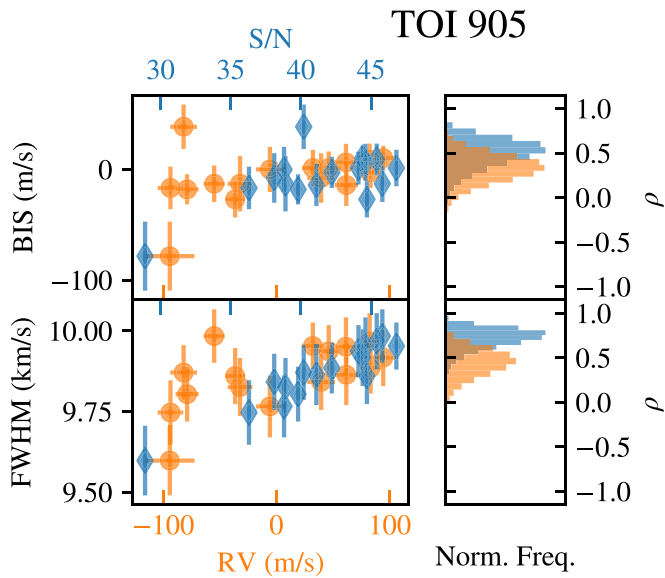


Figure 11. Same as Figure 10 but for TOI 905.

~ 0.1 ppt depth difference between the transit depth in B and V for this star. Indeed, the transit depths between B (3.01 ppt) and z' (3.55 ppt) only differ by $\sim 14\%$. We attribute this slight chromatic dependence to the position of the grazing transit chord, which preferentially covers the reddened limb of the star.

The hierarchical triple-system scenario would similarly cause a color dependence in the RVs due to a varying amount of spectral contamination from the red to the blue wavelengths. To the contrary, we found that RVs as a function of spectral order were distributed randomly, and there is no sign of any color dependence.

5.1.2. Rejecting FP Scenarios for TOI 905 b

For TOI 905, there is a marginally significant correlation between BIS and RV and a highly significant nonzero correlation for FWHM and RV, as shown in Figure 11. Just as with TOI 564, we see that the S/N has a far stronger correlation with both BIS and FWHM; for instance, while the FWHM and RV have a nonzero correlation at the 3.3σ level, the FWHM and S/N have a nonzero correlation at the 9.5σ level. Absent other evidence, we attribute this correlation to our pipeline rather than an astrophysical FP.

Nevertheless, since an extremely significant bisector correlation was detected in the CCFs of TOI 905, we further analyzed these spectra using TODCOR (Zucker & Mazeh 1994). We searched for additional RV components separated by less than $\sim 15 \text{ km s}^{-1}$ in a procedure similar to the one applied in the analysis of the wide binary companion of HD 202772A (Wang et al. 2019). The search revealed no significant secondary velocity signal. TODCOR confirmed that the RV signal was on target and that it was not induced by a blend with another component. The upper limit on the relative flux contribution of another star in the system was estimated to be $\sim 5\%$ – 10% .

An independent reduction of the RVs obtained with TODCOR and BIS measurements obtained with UNICOR (Engel et al. 2017) reproduced the observed RV semi-amplitude using the reduction described in Section 2.4.2 but not the strong CCF correlations found by the CHIRON reduction; this reinforces our conclusion that the correlations (discussed here

and in Section 5.1.1) are dominated by reduction issues and are not astrophysical in origin.

There is a nearby star with $\Delta \text{mag} = 5.9$ located $2''.28$ away from the primary star (see Section 2.3.1). This star is also detected in Gaia DR2 with a parallax of $7.85 \pm 0.55 \text{ mas}$. This value differs by nearly 3σ from the primary star's parallax of $6.27 \pm 0.03 \text{ mas}$, so we assume this is an unrelated background star. If TOI 905 b were an FP BEB, then we would expect that the RV semi-amplitude would depend on the degree of contamination between the foreground and background stars. CHIRON and HARPS have sky fiber radii of $0''.5$ and $1''.35$, respectively, which means that (modulo seeing variations) they should experience different degrees of contamination from this background source. However, the two spectrographs return highly consistent RV semi-amplitude measurements, which rules out the BEB interpretation.

5.2. Characterization from Available Data

Both TOI 564 b and TOI 905 b are classical transiting hot Jupiters orbiting G-type host stars. The former has a period of 1.65 days, mass of $1.46 M_J$, and radius of $\sim 1 R_J$; this radius is poorly determined because of the planet's grazing transit. The latter has a period of 3.74 days, mass of $0.67 M_J$, and radius of $1.17 R_J$. Figure 12 (left) shows these planets' masses and radii compared to other transiting planets. Here TOI 905 b sits comfortably among previously discovered gas giants, as does TOI 564 b, even near the extremes of its 68% CI radius values.

Based on TOI 564 b's calculated T_{eq} of $1714_{-21}^{+20} \text{ K}$, the fact that it is a gas giant-mass planet, and comparison to other known hot Jupiters (see, e.g., Wu et al. 2018), it is likely that TOI 564 b is inflated. A typical hot Jupiter at this T_{eq} would have a radius of $\sim 1.3 R_J$, which is consistent within our measured radius of $1.02_{-0.29}^{+0.71} R_J$. If TOI 564 b's radius fell at the low end of the 68% CI derived from EXOFASTv2, it would be one of the least inflated giant planets, given its temperature. Given the difficulties in modeling a grazing transit, we suggest that TOI 564 b's radius should be viewed cautiously as a lower bound. The object TOI 905 b has a calculated T_{eq} of $1192_{-36}^{+39} \text{ K}$, which puts it just past the critical temperature of inflation ($1123.7 \pm 3.3 \text{ K}$) found by Wu et al. (2018). At $1.17 R_J$, this planet is fully consistent with known giant planets at this T_{eq} .

The high impact parameter, $b = 0.994_{-0.049}^{+0.083}$, makes TOI 564 b stand out in Figure 12 (right), which plots the grazing transit condition versus Gaia magnitude. The star TOI 564 is among the brightest known to host a grazing transiting planet; TOI 905 b has a somewhat large, but decidedly nongrazing, impact parameter as well.

5.3. Potential for Follow-up Observations

5.3.1. Thermal Emission

Planets that undergo eclipses by their host stars allow the thermal emissions of the planets to be directly probed. We find that TOI 564 b is probably not eclipsed by its host star, but this is only ruled out at the 1σ level. Since the planet's primary transit is grazing, a complete secondary eclipse could only occur if there is a slightly eccentric planetary orbit. Absent this scenario, it seems likely that thermal emission spectra taken during a partial eclipse would suffer from the same degeneracies as the planetary radius measurements.

It is expected that TOI 905 b will be eclipsed by its host, with an eclipse duration of $0.0845_{-0.0015}^{+0.0011} \text{ day}$. There is, therefore,

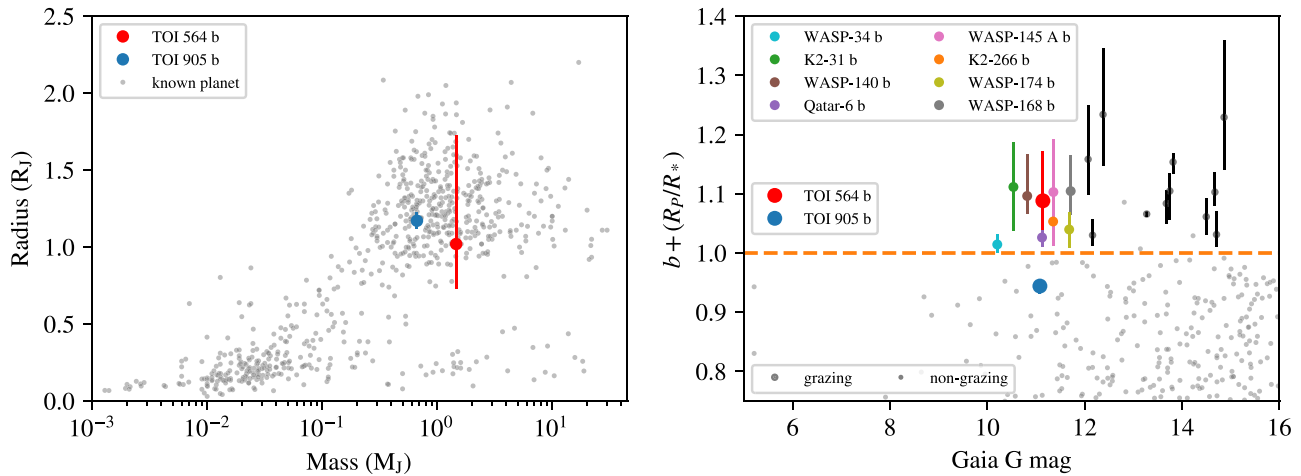


Figure 12. Newly discovered planets TOI 564 b and TOI 905 b compared to known planets that have parameters published in the NASA Exoplanet Archive (accessed 2019 December 15; Akeson et al. 2013). Left: mass–radius relation for confirmed transiting planets, with TOI 564 b and TOI 905 b in red and blue, respectively, with 68% confidence indicated (errors omitted for known planets). Both masses and radii are typical of gas giant planets. Right: grazing transit condition vs. G (Gaia) magnitude. The orange dashed line indicates the threshold above which transits become grazing. Planets with grazing transit probabilities greater than 84% (i.e., based on published 1σ uncertainties) are labeled in various colors or in black. The object TOI 564 is among the brightest stars known to host a grazing transiting planet with high confidence.

potential for further study of this planet’s thermal emission and for atmospheric characterization. At $V = 11.2$, this star is comparable in brightness to other successful secondary eclipse targets (e.g., WASP-12 b; Croll et al. 2015).

5.3.2. RM Measurements

Many transiting hot Jupiters make for good targets for RM measurements of spin–orbit alignment. We simulated the RM effect using ExOSAM (see Addison et al. 2018) for both TOI 564 b and TOI 905 b. Following the results of the TRES observations, we set $V \sin i = 3.5 \text{ km s}^{-1}$ for TOI 564, and we consider two cases: an aligned orbit with $\lambda = 0^\circ$ and a polar orbit with $\lambda = 90^\circ$. For an aligned orbit, the predicted semiamplitude of the velocity anomaly is $\sim 8 \text{ m s}^{-1}$. In the case where $\lambda \sim 90^\circ$ and the star has a nontrivial $V \sin i$, either the redshifted or the blueshifted limb of the star will be occulted, which will result in a measurable, fully asymmetric RM signal of $\sim 7 \text{ m s}^{-1}$. With a transit duration of just over 1 hr, it would be readily possible for a large-aperture telescope with a spectrograph attaining better than 4 m s^{-1} precision with a cadence of ~ 10 minutes (e.g., Keck/HIRES, Vogt et al. 1994; Magellan/PFS, Crane et al. 2006) to measure λ in this system. We do not have measurements of $V \sin i$ for TOI 905, but the deeper transit would probably create a larger RM signal; e.g., arbitrarily assuming the same $V \sin i$ of 3.5 km s^{-1} , we find that TOI 905 b would have an RM semiamplitude of $\sim 23 \text{ m s}^{-1}$ for an aligned orbit.

5.3.3. Exploiting the Grazing Transit of TOI 564 b

As shown in Figure 12, TOI 564 is one of brightest known hosts to a grazing transiting planet, which makes it one of the most attractive targets for long-term monitoring in searches for transit depth and impact parameter variations that could reveal the presence of nontransiting planets or exomoons (Kipping 2009, 2010). Grazing transits also offer an opportunity to search for extrojan asteroids (e.g., Lillo-Box et al. 2018) by exploiting the sensitivity of the orbit of the planet to co-orbital perturbations.

Miralda-Escudé (2002) examined this possibility using the 51 Peg system (Mayor & Queloz 1995) as an example. A close-in hot Jupiter will experience a precession in both its periastron and its line of nodes when an additional planet is present in the system. Miralda-Escudé (2002) found, for example, that in the case of an Earth-mass planet located at $a = 0.2 \text{ au}$ with an inclination of 45° , 51 Peg b would experience transit duration changes of 1 s yr^{-1} , which would be detectable over many years of observation. However, the grazing nature of TOI 564 b’s transit means that any line-of-nodes precession will manifest itself as a change to the already-high impact parameter, upon which the transit duration and transit depth are both extremely sensitive. These changes can be used to dynamically constrain the presence of smaller and more distant planetary companions, which are of particular interest because they can help address hot Jupiter formation and evolution scenarios.

In addition to serving as a probe of other bodies in the system, TOI 564 b may also be a valuable data point in informing the mystery behind the paucity in detections of exoplanets with grazing transits, even after accounting for the detection biases resulting from their shallower and shorter transits. Some of this deficit surely results from human bias in selecting follow-up targets; V-shaped light curves are frequently found to be FPs, which makes them a lower priority for a follow-up program whose goal is to confirm planets. However, there has been speculation that there may be an astrophysical component to the lack of grazing transit detections as well. Polar star spots have been observed on both main-sequence stars (Jeffers et al. 2002) and active, rapid rotators (Schuessler & Solanki 1992). These spots reduce the background flux of the region occulted by planets exhibiting a grazing transit, which necessarily transit at high latitude in the default case of $\lambda = 0^\circ$. Oshagh et al. (2015) posited that this effect could be responsible for the dearth of grazing transiting planet detections by Kepler. If TOI 564 b is indeed a grazing planet in an aligned orbit, then its transits must cross the stellar pole, which would grant us the opportunity to study this phenomenon.

6. Summary and Conclusion

We report the discovery and confirmation of two new hot Jupiters identified by TESS: TOI 564 b and TOI 905 b. The former is noteworthy in that it displays a grazing transit across its Sun-like host star over its 1.65 day orbit. Both targets are main-sequence G stars that are relatively bright ($V \sim 11$), making them good targets for follow-up characterization.

Both planets were validated based on TESS light curves, ground-based photometry in multiple filters, and robust RV detections by two different spectrographs. Both stars were observed with speckle interferometry (HRCam/SOAR), and TOI 564 was also observed with PHARO/Hale AO; it is a probable binary system, with an M-dwarf companion at a projected distance of ~ 100 au.

We conducted multiple independent measurements of the host stars' stellar parameters using the high-resolution CHIRON and TRES spectra, as well as an SED analysis, and found a general agreement between the derived parameters. Using the EXOFASTv2 planet fitting suite, we ran a global analysis by simultaneously fitting the transit and RV data with an MCMC. The impact parameter of TOI 564 b was found to be near unity, diminishing our ability to constrain its radius, but its mass, as well as the radius and mass of TOI 905 b, was measured with high precision.

We explored and rejected a variety of FP scenarios (e.g., BEB or NEB) for both systems. We conducted simulations of the RM effect for each system, and we found that both planets should produce detectable RM signals. It is expected that TOI 905 b will undergo secondary eclipses and therefore be amenable to thermal emission measurement; TOI 564 b probably does not experience secondary eclipses. We noted that the unique sensitivity of grazing transits to small orbital perturbations may be exploited to search TOI 564 (one of the brightest known grazing transit hosts) for additional nontransiting bodies, and also that the grazing transit offers the opportunity to study polar star spots.

A.B.D. is supported by the National Science Foundation Graduate Research Fellowship Program under grant No. DGE-1122492. S.W. thanks the Heising-Simons Foundation for its generous support as a 51 Pegasi b fellow. M.N.G. acknowledges support from MIT's Kavli Institute as a Torres postdoctoral fellow. C.Z. is supported by a Dunlap Fellowship at the Dunlap Institute for Astronomy & Astrophysics, funded through an endowment established by the Dunlap family and the University of Toronto. Work by J.N.W. was partly supported by the Heising-Simons Foundation. This work is partly supported by JSPS KAKENHI grant Nos. JP18H01265 and JP18H05439 and JST PRESTO grant No. JPMJPR1775. H.P. and E.P. acknowledge funding from the Spanish Ministry of Economics and Competitiveness through project PGC2018-098153-B-C31.

Funding for the TESS mission is provided by the National Aeronautics and Space Administration's (NASA) Science Mission directorate. We acknowledge the use of public TESS Alert data from pipelines at the TESS Science Office and the TESS Science Processing Operations Center. Resources supporting this work were provided by the NASA High-End Computing (HEC) Program through the NASA Advanced Supercomputing (NAS) Division at Ames Research Center for the production of the SPOC data products. This research has made use of the Exoplanet Follow-up Observation Program

website and the NASA Exoplanet Archive, which is operated by the California Institute of Technology, under contract with the National Aeronautics and Space Administration under the Exoplanet Exploration Program. This paper includes data collected by the TESS mission, which are publicly available from the Mikulski Archive for Space Telescopes (MAST).

Part of this research was carried out at the Jet Propulsion Laboratory, California Institute of Technology, under a contract with NASA.

This work makes use of observations from SMARTS and the LCOGT network.


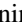
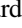

This work is based on observations collected at the European Organisation for Astronomical Research in the Southern Hemisphere under ESO program 0103.C-0548.



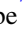




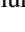

This work is based on observations made with the MuSCAT2 instrument, developed by ABC, at Telescopio Carlos Sánchez, operated on the island of Tenerife by the IAC in the Spanish Observatorio del Teide.

Software: numpy (van der Walt et al. 2011), pandas (Reback et al. 2020), emcee (Foreman-Mackey et al. 2013, 2018), celerite (Foreman-Mackey et al. 2017a, 2017b), EXOFAST (v2; Eastman et al. 2013; Eastman 2017; Eastman et al. 2019), Tapir software package (Jensen 2013), AstroImageJ (Collins et al. 2017), ARES2 (v2; Sousa et al. 2015), MOOG code (Snedden 1973).

Facilities: TESS, CTIO:1.5 m (CHIRON), FLWO:1.5 m (TRES), ESO:3.6 m (HARPS), LCOGT, Sanchez (MuSCAT2), SOAR (HRCam), Hale (PHARO).

ORCID iDs

Allen B. Davis  <https://orcid.org/0000-0002-5070-8395>
 Songhu Wang  <https://orcid.org/0000-0002-7846-6981>
 Jason D. Eastman  <https://orcid.org/0000-0003-3773-5142>
 Maximilian N. Günther  <https://orcid.org/0000-0002-3164-9086>
 Keivan G. Stassun  <https://orcid.org/0000-0002-3481-9052>
 Brett C. Addison  <https://orcid.org/0000-0003-3216-0626>
 Karen A. Collins  <https://orcid.org/0000-0001-6588-9574>
 Samuel N. Quinn  <https://orcid.org/0000-0002-8964-8377>
 David W. Latham  <https://orcid.org/0000-0001-9911-7388>
 Trifon Trifonov  <https://orcid.org/0000-0002-0236-775X>
 Tsevi Mazeh  <https://orcid.org/0000-0002-3569-3391>
 Stephen R. Kane  <https://orcid.org/0000-0002-7084-0529>
 Norio Narita  <https://orcid.org/0000-0001-8511-2981>
 Xian-Yu Wang  <https://orcid.org/0000-0002-0376-6365>
 Thiam-Guan Tan  <https://orcid.org/0000-0001-5603-6895>
 David R. Ciardi  <https://orcid.org/0000-0002-5741-3047>
 Andrei Tokovinin  <https://orcid.org/0000-0002-2084-0782>
 Carl Ziegler  <https://orcid.org/0000-0002-0619-7639>
 René Tronsgaard  <https://orcid.org/0000-0003-1001-0707>
 Sarah Millholland  <https://orcid.org/0000-0003-3130-2282>
 Michael L. Calkins  <https://orcid.org/0000-0002-2830-5661>
 Gilbert A. Esquerdo  <https://orcid.org/0000-0002-9789-5474>
 Kevin I. Collins  <https://orcid.org/0000-0003-2781-3207>
 Dennis M. Conti  <https://orcid.org/0000-0003-2239-0567>
 Phil Evans  <https://orcid.org/0000-0002-5674-2404>
 Pablo Lewin  <https://orcid.org/0000-0003-0828-6368>
 Todd J. Henry  <https://orcid.org/0000-0002-9061-2865>
 Michael B. Lund  <https://orcid.org/0000-0003-2527-1598>
 Jessie L. Christiansen  <https://orcid.org/0000-0002-8035-4778>

Nicholas M. Law  <https://orcid.org/0000-0001-9380-6457>
 Andrew W. Mann  <https://orcid.org/0000-0003-3654-1602>
 Hannu Parviainen  <https://orcid.org/0000-0001-5519-1391>
 Enric Palle  <https://orcid.org/0000-0003-0987-1593>
 Noriharu Watanabe  <https://orcid.org/0000-0002-7522-8195>
 George R. Ricker  <https://orcid.org/0000-0003-2058-6662>
 Roland Vanderspek  <https://orcid.org/0000-0001-6763-6562>
 Sara Seager  <https://orcid.org/0000-0002-6892-6948>
 Joshua N. Winn  <https://orcid.org/0000-0002-4265-047X>
 Jon M. Jenkins  <https://orcid.org/0000-0002-4715-9460>
 Akshata Krishnamurthy  <https://orcid.org/0000-0002-8781-2743>
 Natalie M. Batalha  <https://orcid.org/0000-0002-7030-9519>
 Jennifer Burt  <https://orcid.org/0000-0002-0040-6815>
 Knicole D. Colón  <https://orcid.org/0000-0001-8020-7121>
 Scott Dynes  <https://orcid.org/0000-0001-7010-0937>
 Douglas A. Caldwell  <https://orcid.org/0000-0003-1963-9616>
 Debra A. Fischer  <https://orcid.org/0000-0003-2221-0861>

References

- Adams, F. C., & Laughlin, G. 2006, *ApJ*, **649**, 1004
 Addison, B. C., Wang, S., Johnson, M. C., et al. 2018, *AJ*, **156**, 197
 Akeson, R. L., Chen, X., Ciardi, D., et al. 2013, *PASP*, **125**, 989
 Albrecht, S., Winn, J. N., Marcy, G. W., et al. 2013, *ApJ*, **771**, 11
 Almenara, J. M., Bouchy, F., Gault, P., et al. 2013, *A&A*, **555**, A118
 Almenara, J. M., Damiani, C., Bouchy, F., et al. 2015, *A&A*, **575**, A71
 Alonso, A., Arribas, S., & Martínez-Roger, C. 1999, *A&AS*, **140**, 261
 Alonso, R., Barbieri, M., Rabus, M., et al. 2008, *A&A*, **487**, L5
 Alsubai, K., Tsvetanov, Z. I., Latham, D. W., et al. 2018, *AJ*, **155**, 52
 Anderson, D. R., Barros, S. C. C., Boisse, I., et al. 2011, *PASP*, **123**, 555
 Anderson, D. R., Collier Cameron, A., Gillon, M., et al. 2012, *MNRAS*, **422**, 1988
 Bakos, G., Noyes, R. W., Kovács, G., et al. 2004, *PASP*, **116**, 266
 Batygin, K., Bodenheimer, P. H., & Laughlin, G. P. 2016, *ApJ*, **829**, 114
 Bayliss, D., Gillen, E., Eiglmüller, P., et al. 2018, *MNRAS*, **475**, 4467
 Bean, J. L., & Seifahrt, A. 2008, *A&A*, **487**, L25
 Becker, J. C., Vanderburg, A., Adams, F. C., Rappaport, S. A., & Schwengel, H. M. 2015, *ApJL*, **812**, L18
 Béky, B., Bakos, G. Á., Hartman, J., et al. 2011, *ApJ*, **734**, 109
 Bodenheimer, P., Hubickyj, O., & Lissauer, J. J. 2000, *Icar*, **143**, 2
 Borucki, W. J., Koch, D., Basri, G., et al. 2010, *Sci*, **327**, 977
 Bressan, A., Marigo, P., Girardi, L., et al. 2012, *MNRAS*, **427**, 127
 Brown, T. M., Baliber, N., Bianco, F. B., et al. 2013, *PASP*, **125**, 1031
 Bruno, G., Lewis, N. K., Stevenson, K. B., et al. 2018, *AJ*, **155**, 55
 Buchhave, L. A., Bakos, G. Á., Hartman, J. D., et al. 2010, *ApJ*, **720**, 1118
 Buchhave, L. A., Latham, D. W., Johansen, A., et al. 2012, *Natur*, **486**, 375
 Butler, R. P., Vogt, S. S., Marcy, G. W., et al. 2004, *ApJ*, **617**, 580
 Cañas, C. I., Stefansson, G., Monson, A. J., et al. 2019a, *ApJL*, **877**, L29
 Cañas, C. I., Wang, S., Mahadevan, S., et al. 2019b, *ApJL*, **870**, L17
 Choi, J., Dotter, A., Conroy, C., et al. 2016, *ApJ*, **823**, 102
 Claret, A. 2018, *A&A*, **618**, A20
 Collins, K. A., Collins, K. I., Pepper, J., et al. 2018, *AJ*, **156**, 234
 Collins, K. A., Kielkopf, J. F., Stassun, K. G., & Hessman, F. V. 2017, *AJ*, **153**, 77
 Crane, J. D., Shtetman, S. A., & Butler, R. P. 2006, *Proc. SPIE*, **6269**, 626931
 Crida, A., & Batygin, K. 2014, *A&A*, **567**, A42
 Croll, B., Albert, L., Jayawardhana, R., et al. 2015, *ApJ*, **802**, 28
 Cutri, R. M., Skrutskie, M. F., van Dyk, S., et al. 2003, *yCat*, **2246**, 0
 Cutri, R. M. 2013, *yCat*, **2328**, 0
 Dawson, R. I., Huang, C. X., Lissauer, J. J., et al. 2019, *AJ*, **158**, 65
 Demory, B. O., Gillon, M., Waelkens, C., Queloz, D., & Udry, S. 2009, in IAU Symp. 253, *Transiting Planets*, ed. F. Pont, D. Sasselov, & M. J. Holman (Cambridge: Cambridge Univ. Press), 424
 Dong, S., Katz, B., & Socrates, A. 2014, *ApJL*, **781**, L5
 Dotter, A. 2016, *ApJS*, **222**, 8
 Eastman, J. 2017, EXOFASTv2: Generalized publication-quality exoplanet modeling code, Astrophysics Source Code Library, ascl:1710.003
 Eastman, J., Gaudi, B. S., & Agol, E. 2013, *PASP*, **125**, 83
 Eastman, J. D., Rodriguez, J. E., Agol, E., et al. 2019, arXiv:1907.09480
 Engel, M., Shahaf, S., & Mazeh, T. 2017, *PASP*, **129**, 065002
 Fűrész, G., Szentgyorgyi, A. H., & Meibom, S. 2008, in *Precision Spectroscopy in Astrophysics*, ed. N. C. Santos et al. (Berlin: Springer), 287
 Fischer, D. A., & Valenti, J. 2005, *ApJ*, **622**, 1102
 Ford, E. B., & Rasio, F. A. 2008, *ApJ*, **686**, 621
 Foreman-Mackey, D., Agol, E., Ambikasaran, S., & Angus, R. 2017a, *AJ*, **154**, 220
 Foreman-Mackey, D., Agol, E., Angus, R., et al. 2017b, Dfm/Celerite: Celerite V0.3.0, Zenodo, doi:10.5281/zenodo.1048287
 Foreman-Mackey, D., Hogg, D. W., Lang, D., & Goodman, J. 2013, *PASP*, **125**, 306
 Foreman-Mackey, D., Meierjürgen Farr, W., Tollerud, E., et al. 2018, Dfm/Emcee: Emcee V3.0Rc2, Zenodo, doi:10.5281/zenodo.1436565
 Fressin, F., Torres, G., Charbonneau, D., et al. 2013, *ApJ*, **766**, 81
 Gaia Collaboration, Brown, A. G. A., Vallenari, A., et al. 2018, *A&A*, **616**, A1
 Grziwa, S., Gandolfi, D., Csizmadia, S., et al. 2016, *AJ*, **152**, 132
 Günther, M. N., Queloz, D., Gillen, E., et al. 2017, *MNRAS*, **472**, 295
 Günther, M. N., Queloz, D., Gillen, E., et al. 2018, *MNRAS*, **478**, 4720
 Hayward, T. L., Brandl, B., Pirger, B., et al. 2001, *PASP*, **113**, 105
 Hellier, C., Anderson, D. R., Cameron, A. C., et al. 2017, *MNRAS*, **465**, 3693
 Hellier, C., Anderson, D. R., Collier Cameron, A., et al. 2012, *MNRAS*, **426**, 739
 Høg, E., Fabricius, C., Makarov, V. V., et al. 2000, *A&A*, **355**, L27
 Holt, J. R. 1893, *AstAp*, **12**, 646
 Howard, A. W., Marcy, G. W., Bryson, S. T., et al. 2012, *ApJS*, **201**, 15
 Howell, S. B., Soback, C., Haas, M., et al. 2014, *PASP*, **126**, 398
 Huang, C., Wu, Y., & Triaud, A. H. M. J. 2016, *ApJ*, **825**, 98
 Jeffers, S. V., Barnes, J. R., & Collier Cameron, A. 2002, *MNRAS*, **331**, 666
 Jenkins, J. M., Twicken, J. D., McCauliff, S., et al. 2016, *Proc. SPIE*, **9913**, 99133E
 Jensen, E. 2013, Tapir: A web interface for transit/eclipse observability, Astrophysics Source Code Library, ascl:1306.007
 Jones, M. I., Brahm, R., Espinoza, N., et al. 2019, *A&A*, **625**, A16
 Jones, M. I., Brahm, R., Wittenmyer, R. A., et al. 2017, *A&A*, **602**, A58
 Jones, M. I., Jenkins, J. S., Rojo, P., & Melo, C. H. F. 2011, *A&A*, **536**, A71
 Kipping, D. M. 2009, *MNRAS*, **396**, 1797
 Kipping, D. M. 2010, *MNRAS*, **407**, 301
 Knutson, H. A., Fulton, B. J., Montet, B. T., et al. 2014, *ApJ*, **785**, 126
 Kossakowski, D., Espinoza, N., Brahm, R., et al. 2019, *MNRAS*, **490**, 1094
 Kurucz, R. 1993, ATLAS9 Stellar Atmosphere Programs and 2 km/s grid, CD-ROM No. 13 (Cambridge, MA: Smithsonian Astrophysical Observatory)
 Lillo-Box, J., Barrado, D., Figueira, P., et al. 2018, *A&A*, **609**, A96
 Lillo-Box, J., Barrado, D., Santos, N. C., et al. 2015, *A&A*, **577**, A105
 Lin, D. N. C., Bodenheimer, P., & Richardson, D. C. 1996, *Natur*, **380**, 606
 Mancini, L., Sarkis, P., Henning, T., et al. 2020, *A&A*, **633**, A30
 Mayor, M., Pepe, F., Queloz, D., et al. 2003, *Msngr*, **114**, 20
 Mayor, M., & Queloz, D. 1995, *Natur*, **378**, 355
 McLaughlin, D. B. 1924, *ApJ*, **60**, 22
 Millholland, S., Wang, S., & Laughlin, G. 2016, *ApJL*, **823**, L7
 Miralda-Escudé, J. 2002, *ApJ*, **564**, 1019
 Naoz, S., Farr, W. M., Lithwick, Y., Rasio, F. A., & Teysandier, J. 2011, *Natur*, **473**, 187
 Narita, N., Fukui, A., Kusakabe, N., et al. 2019, *JATIS*, **5**, 015001
 Öberg, K. I., Murray-Clay, R., & Bergin, E. A. 2011, *ApJL*, **743**, L16
 Oshagh, M., Santos, N. C., Figueira, P., et al. 2015, *A&A*, **583**, L1
 Parviainen, H., Tingley, B., Deeg, H. J., et al. 2019, *A&A*, **630**, A89
 Petigura, E. A., Marcy, G. W., Winn, J. N., et al. 2018, *AJ*, **155**, 89
 Pont, F., Gilliland, R. L., Knutson, H., Holman, M., & Charbonneau, D. 2009, *MNRAS*, **393**, L6
 Queloz, D., Eggenberger, A., Mayor, M., et al. 2000, *A&A*, **359**, L13
 Reback, J., McKinney, W., & Mendel, B. J. 2020, pandas-dev/pandas: Pandas 1.0.0, v1.0.0, Zenodo, doi:10.5281/zenodo.3630805
 Ribas, I., Font-Ribera, A., & Beaulieu, J.-P. 2008, *ApJL*, **677**, L59
 Ricker, G. R., Winn, J. N., Vanderspek, R., et al. 2015, *JATIS*, **1**, 014003
 Rodriguez, J. E., Quinn, S. N., Huang, C. X., et al. 2019, *AJ*, **157**, 191
 Rossiter, R. A. 1924, *ApJ*, **60**, 15
 Schlafly, E. F., & Finkbeiner, D. P. 2011, *ApJ*, **737**, 103
 Schlegel, D. J., Finkbeiner, D. P., & Davis, M. 1998, *ApJ*, **500**, 525
 Schlesinger, F. 1910, *PALIO*, **1**, 123
 Schuessler, M., & Solanki, S. K. 1992, *A&A*, **264**, L13
 Sing, D. K., Fortney, J. J., Nikolov, N., et al. 2016, *Natur*, **529**, 59
 Smalley, B., Anderson, D. R., Collier Cameron, A., et al. 2011, *A&A*, **526**, A130
 Smith, J. C., Stumpe, M. C., Van Cleve, J. E., et al. 2012, *PASP*, **124**, 1000

- Snedden, C. 1973, *ApJ*, **184**, 839
- Sousa, S. G., Santos, N. C., Adibekyan, V., Delgado-Mena, E., & Israelian, G. 2015, *A&A*, **577**, A67
- Stassun, K. G., Collins, K. A., & Gaudi, B. S. 2017, *AJ*, **153**, 136
- Stassun, K. G., Corsaro, E., Pepper, J. A., & Gaudi, B. S. 2018a, *AJ*, **155**, 22
- Stassun, K. G., Oelkers, R. J., Pepper, J., et al. 2018b, *AJ*, **156**, 102
- Stassun, K. G., & Torres, G. 2016, *AJ*, **152**, 180
- Stassun, K. G., & Torres, G. 2018, *ApJ*, **862**, 61
- Stumpe, M. C., Smith, J. C., Catanzarite, J. H., et al. 2014, *PASP*, **126**, 100
- Temple, L. Y., Hellier, C., Almléaky, Y., et al. 2018, *MNRAS*, **480**, 5307
- Tokovinin, A. 2018, *PASP*, **130**, 035002
- Tokovinin, A., Fischer, D. A., Bonati, M., et al. 2013, *PASP*, **125**, 1336
- Torres, G., Andersen, J., & Giménez, A. 2010, *A&A Rv*, **18**, 67
- Torres, G., Konacki, M., Sasselov, D. D., & Jha, S. 2004, *ApJ*, **614**, 979
- Twicken, J. D., Catanzarite, J. H., Clarke, B. D., et al. 2018, *PASP*, **130**, 064502
- van der Walt, S., Colbert, S. C., & Varoquaux, G. 2011, *CSE*, **13**, 22
- Vogt, S. S., Allen, S. L., Bigelow, B. C., et al. 1994, *Proc. SPIE*, **2198**, 362
- Wang, S., Addison, B., Fischer, D. A., et al. 2018, *AJ*, **155**, 70
- Wang, S., Jones, M., Shporer, A., et al. 2019, *AJ*, **157**, 51
- Winn, J. N. 2009, in IAU Symp. 253, *Transiting Planets*, ed. F. Pont, D. Sasselov, & M. J. Holman (Cambridge: Cambridge Univ. Press), 99
- Winn, J. N., & Fabrycky, D. C. 2015, *ARA&A*, **53**, 409
- Wu, D.-H., Wang, S., Zhou, J.-L., Steffen, J. H., & Laughlin, G. 2018, *AJ*, **156**, 96
- Wu, Y., & Lithwick, Y. 2011, *ApJ*, **735**, 109
- Zhou, G., Huang, C. X., Bakos, G. Á., et al. 2019, *AJ*, **158**, 141
- Ziegler, C., Tokovinin, A., Briceño, C., et al. 2020, *AJ*, **159**, 19
- Zucker, S., & Mazeh, T. 1994, *ApJ*, **420**, 806